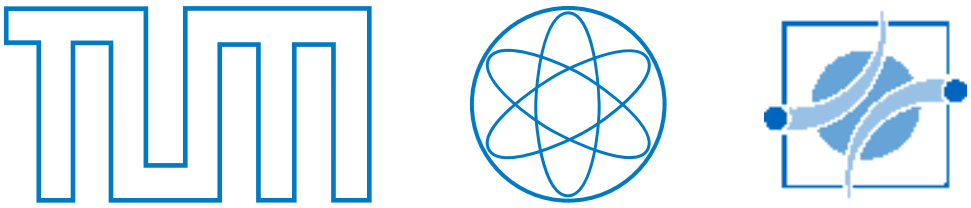

Technische Universität München
Physics Departement
Institute for Experimental Physics E12

Abschlussarbeit im Bachelorstudiengang Physik

Characterization of three HPGe detectors for a Doppler shift attenuation experiment

Rupert Patrick Heider

Garching, den 25. Juli 2011

Betreuer: Prof. Dr. Shawn Bishop

Erstgutachter (Themensteller): Prof. Dr. Shawn Bishop

Zweitgutachter: .....

Contents

List of Figures

List of Tables

Chapter 1

Introduction

In 1572 the astronomer Tycho Brahe observed a suddenly emerged, previously invisible star-like object in the sky and termed it *stella nova* (Latin for "new star"). In his work he argued that a nova had to be very far away, because a nearby object should be seen to move relative to the fixed stars. Though he had observed a supernova and not a classical nova, the terms were considered interchangeable until the 1930s, but today a supernova and a nova are known to be two different events in our universe[3].

Nowadays a classical nova denotes a cataclysmic nuclear explosion on the surface of a white dwarf in a binary star system. It is caused by the transfer of hydrogen onto the surface of the white dwarf from a red giant or main sequence companion. This transfer ignites and starts a thermonuclear runaway. Novae are one of the most frequent stellar explosions. Astronomers estimate that in the Milky Way there are roughly 30 to 60 novae per year, with a likely rate of about 40[3].
Mostly, the hydrogen burning is thermally unstable, so it rapidly converts a large amount of the hydrogen into other heavier elements in a series of nuclear reactions. This implies that, in classical novae outbursts, elements with a mass up to $A = 40$ can be built by proton capture processes. In resonant nuclear reactions that are promoted by the physical conditions (far away from equilibrium) particular isotopes, which are not possible to be formed within other events in the universe, are synthesized and blown off into the space. Examples for these isotopes are ^{7}Li, ^{13}C, ^{15}N, ^{17}O and in special special cases ^{26}Al, ^{32}S, ^{33}S and ^{35}Cl[4].

Therefore, nuclear reactions in novae explosions play an important role in the production of elements that are the basis of our existence and are necessary for the life on earth. These resonant nuclear reactions play a leading part in the reaction processes in novae, making them essential for the theoretical understanding and physical models of a nova outburst.

One of the important properties characterizing resonant reaction rates are the life times of exited states in compound nuclei formed by proton capture. An applicable experimental technique to determine these life times is the so-called *Doppler shift attenuation method* (DSAM) which has been successfully used to measure life times of excited nuclear states between around 10^{-14} and $10^{-11}s$. The central idea of this method is the analysis of the Doppler shift that can be detected in the gamma ray spectrum of the decays of ions that are produced in excited states and immediately decelerated rapidly in a heavy target material.

The purpose of the DSAM experimental facility that is set up by the experimental astrophysics group at the Maier-Leibniz-Laboratory (MLL) located on the Garching campus of the Technische Universität München is to measure the life times of the excited states in proton rich nuclei of masses that range between $A = 20$ and $A = 40$. At the laboratory there is a Van-de-Graaff tandem accelerator that achieves a maximum operating potential of 14 MV. The accelerator's ion beam is used for producing excited nuclei of astrophysical interest in an implantation layer of the target and stopping this nucleus within the target itself. The Doppler shifted gamma ray spectrum is recorded applying three high purity germanium (HPGe) gamma ray detectors. Furthermore, coincidence measurements with light ejectiles and the de-excitation γ-rays are done with the help of a silicon detector $\Delta E - E$ telescope.

Within the frame of this bachelor's thesis the three HPGe detectors, positioned at different angles around the target chamber, are calibrated and characterized as it is necessary for the usage within the DSAM experiment, particularly for the precise analysis of the gamma ray spectra. For each of the three detectors the Photopeaks of overall three different sources of radiation are fitted by a complex mathematical function in order to determine the response function, the Photopeak efficiency and the intrinsic efficiency dependent on the energy. Furthermore, an energy calibration for the three detectors is performed.
In Chapter two initially the theoretical fundamentals of resonant reaction rates, the general basics of the DSAM experiment as well as general considerations about HPGe detectors are described.
The applied methods of the characterization and the approach to the calibration of the three HPGe detectors are presented in chapter 3 and the measurement results are analyzed.
In chapter 4 the thesis is concluded with a brief summary of the results and an outlook to a further use of the data is provided.

Chapter 2

Basics

2.1 Nuclear Reaction Rates in Novae

In this section will present some basic physical principles of thermonuclear resonant reaction rates.

2.1.1 Kinematics and Energetics

Particle a strikes a nucleus X producing the nucleus Y and the particle b. This reaction can be typified by

$$a + X \rightarrow Y + b \tag{2.1}$$

An alternative notation in common usage is

$$X\,(a,b)\,Y \tag{2.2}$$

In such a nuclear reaction the total energy, the angular momentum and also the momentum are conserved quantities. As well-known from classical mechanics, the total energy or momentum of the system is expressed as the energy or momentum of the motion of the center-of-mass system (CMS) plus the sum of the energy or momentum in the CMS. For particles a and X with masses m_a and m_X and non-relativistic velocities v_a and v_X, the velocity of the CMS is given by

$$V = \frac{m_a v_a + m_X v_X}{m_a + m_X} \tag{2.3}$$

In the CMS the so called reduced mass is given by

$$\mu = \frac{m_a m_X}{m_a + m_X} \tag{2.4}$$

and the relative velocity v between particle a and X is

$$v = v_a - v_X \tag{2.5}$$

Because in the CMS the total momentum is zero, particles a and X have equal but opposite momenta. So we demand that the total momentum is zero also after the collision. The kinetic energy before the collision is given by

$$E_{CM} = \frac{1}{2} m_a v_a^2 + \frac{1}{2} m_X v_X^2 \tag{2.6}$$

which can be written also as

$$E_{CM} = \frac{1}{2} \left(m_a + m_X \right) V^2 + \frac{1}{2} \mu v^2 \tag{2.7}$$

The first term in the equation above gives us the kinetic energy of the Center of mass itself; the second term is called the kinetic energy in the CMS. In our reaction the principle of conservation-of-energy counts, which is expressed in the following formula:

$$E_a + E_X + \left(M_a + M_X \right) c^2 = E_b + E_Y + \left(M_b + M_Y \right) c^2 \tag{2.8}$$

which is the Einstein mass-energy relationship[5].

2.1.2 Cross Section and Reaction Rate

The energy-balance equation yields the energy that is liberated by each nuclear reaction. The concept of the cross section is used to express the likelihood of interaction between particles. We can define it as

$$\sigma = \frac{\text{Number of reactions per nucleus per unit time}}{\text{Number of incident particles per square centimeter and unit time}} \tag{2.9}$$

The reaction rate between two particles can be written as

$$r = \sigma \left(v \right) v N_a N_X \tag{2.10}$$

where v is the relative velocity between the two particles and N_a and N_X are their particle number densities.

Generalizing equation (2.10), the reaction rate for a distribution of relative velocities is

$$r_{aX} = N_a N_X \left\langle \sigma v \right\rangle_{aX} \tag{2.11}$$

where $\left\langle \sigma v \right\rangle_{aX}$ is the reaction rate per particle pair.

The relative velocity can be described by a Maxwell-Boltzmann distribution and is theoretically distributed between zero and infinity. This velocity distribution has a maximum at $v_m = \sqrt{2kT/\mu}$, which corresponds to an energy of $E = kT$.

For the reaction rate per particle pair one obtains[4]

$$\langle \sigma v \rangle_{aX} = \left(\frac{8}{\pi\mu}\right)^{1/2} \frac{1}{(kT)^{3/2}} \int_0^\infty E\, \sigma(E)\, e^{-E/kT} dE \tag{2.12}$$

where T is the temperature, μ is the reduced mass and k is the Boltzmann constant.

On the reaction cross section there is set a upper bound by the quantum mechanical scattering theory: The 'geometrical factor', $\pi\lambda^2$, with the De Broglie wavelength

$$\lambda = \frac{h}{p} = \frac{2\pi}{k} \tag{2.13}$$

where k is the wave number and p the momentum of the particle. The geometrical factor depends on the energy as:

$$\pi\lambda^2 \sim \left(\frac{1}{p}\right) \sim \frac{1}{E} \tag{2.14}$$

The factor intends to describe the incident particle wave function and the outgoing scattered wave [5].

2.1.3 Compound Nuclear States

As well-known, nucleons cluster into bound states with a discrete energy and a quantized angular momentum that is composed of the orbital and the spin momenta of the constituent nucleons. As we know from atoms, states are not quite stationary because of interactions leading to transitions between the single states. Each state has a width in energy given by

$$\Gamma = \frac{\hbar}{\tau} \tag{2.15}$$

and a energy profile

$$P(E) = \frac{\hbar}{2\pi\tau} \frac{1}{(E - E_i)^2 + \left(\frac{\hbar}{2\tau}\right)^2} \tag{2.16}$$

where τ is the mean lifetime of the decaying state.

If the lifetime of a state is long enough the state's width Γ is sufficiently small (compared to the energy difference between the states) so we can use approximations of stationary energy eigenstates[5]. The nuclear shell model is one of the most successful for the interpretation of nuclear states.
Certain nuclear reactions between two particles (e.g. nuclei) A and B can go through a excited state of a compound nucleus Y^*, so think of the reaction above

$$a + X \rightarrow Y^* \rightarrow Y + b \tag{2.17}$$

Notably Y^* has precisely defined nuclear orbitals which can be populated by the reaction.
A resonance in a nucleus can occur if the combination of the quantum numbers of the particles a and X fits properly to those which are necessary to build the compound nucleus in one of its natural (excited) states above the threshold energy of the reaction, the so-called Q value. Or in other words, the relative kinetic energy of the particles at infinity must be just such that this energy equals that of the populated quasi-stationary state in the compound nucleus.

Because energy and momentum have to be conserved in the formation of the excited state, the sum of the kinetic energy of the particles a and X in the center-of-mass system (so the relative energy) must be identical to the resonance energy E_{res} of an excited state of the nucleus, so[5]

$$E_{CM} = E_{res} = \frac{1}{2}\mu v^2 \tag{2.18}$$

Thus the Q value accrues from

$$E_{CM} = E_C^* - Q \tag{2.19}$$

where E_C^* is the excitation energy of the excited state C^*. Consequently the minimal excitation energy $E_{C,min}^*$ is equal to the Q value:

$$E_{C,min}^* = Q \tag{2.20}$$

Additionally, the angular momentum also has to be conserved which means that

$$\vec{J} = \vec{J_a} + \vec{J_x} + \vec{l} \tag{2.21}$$

is required. $\vec{l}$ is the orbital angular momentum of a and X, J is the angular momentum of the excited state that is supposed to be occupied and J_a and J_b are the spins of the nuclei[5].
Furthermore, the number of possible resonances into which capture is allowed is limited by the fact that parity must be conserved as well:

$$\pi\left(C^*\right) = \pi\left(a\right)\pi\left(X\right)\left(-1\right)^l \tag{2.22}$$

where l is the relative angular momentum of a and X.

2.1.4 The Resonant Reaction Rate

Normally, the stellar reaction rate is dominated by the quasi-stationary states in the compound nuclei (resonances) because their cross sections are much greater than non-resonant direct capture. The cross section of the net reaction from a and X to b and Y is dependent on the quantity of different decay channels for the compound nucleus C, and the probability that C decays into the desired decay channel.
According to quantum mechanics, the maximum value of the l-wave reaction cross section is[5]

$$\sigma_{r,l}\left(max\right) = \left(2l+1\right)\pi\bar{\lambda}^2 \tag{2.23}$$

where $\pi\bar{\lambda}^2$ is the de Broglie geometrical cross section.

Referring to the decay channel 1, the partial width of C is defined as

$$\Gamma_1 = \frac{\hbar}{\tau_1} \tag{2.24}$$

with the lifetime τ_1 of the excited state in C referred to the decay channel 1.
This equation can be regarded as a expression of the principle of uncertainty: The uncertainty of the state's life time (uncertainty in time) multiplied by the width of the state (uncertainty in energy) has to be smaller or at most equal to $\hbar$. The full decay width Γ of an excited state with different decay channels 1,2,3,... is

$$\Gamma = \Gamma_1 + \Gamma_2 + \Gamma_3 + \ldots \tag{2.25}$$

Regarding a state that can decay by just two channels Γ_1 and Γ_2, the total resonant cross section is proportional to the factor

$$\sigma_{res} \propto \Gamma_1 \cdot \left(\Gamma - \Gamma_1\right) \tag{2.26}$$

The total width is linked to the circumstance that the energy of the state is undefined whereas the probability that the state has the energy E is given by equation (2.16). The probability is also proportional to the rate of building the state with particles of energy E. Additionally, being induced by particle 1, the cross section has to be proportional to Γ_1. Therefore the cross section of a resonant reaction ($E = E_{res}$) has to be proportional to

$$\sigma_{res} \propto \Gamma_1 \cdot \left(\Gamma - \Gamma_1\right) P\left(E_{res}\right) \tag{2.27}$$

where $P\left(E_{res}\right)$ is given by equation (2.16).
Because the maximum value of the factors in equation (2.26) is unity, we have to multiply these factors by the maximum value of the reaction cross section. Therefore the cross section of the reaction for the l-partial-wave is[5]

$$\sigma_{res,l} = \left(2l+1\right)\pi\bar{\lambda}^2 \frac{\Gamma_1\left(\Gamma - \Gamma_1\right)}{\left(E - E_{res}\right)^2 + \left(\frac{\Gamma}{2}\right)^2} \tag{2.28}$$

The $(\Gamma - \Gamma_1)$ stands for the sum of all partial widths of the decay channels different from the one which formed this state. Finally, one gets the reaction cross section for the products $b + Y$ (in the reaction $a + X \to C^* \to b + Y$) by using just the partial width for that channel:

$$\sigma_{res,l}(a,b) = (2l+1)\,\pi\bar{\lambda}^2 \frac{\Gamma_a \Gamma_b}{(E - E_{res})^2 + \left(\frac{\Gamma}{2}\right)^2} \tag{2.29}$$

This equation is called the single level Breit-Wigner formula[5].
However, it does not yet take the spin of the particles into account. Each spin state J is in accordance with $(2J+1)$ orbital sub-states; every state has a magnetic orbital number m that goes from $-J$ to J. In general two particles 1 and 2 have a total number of $(2J_1+1) \times (2J_2+1)$ potential sub-states.
But the angular momentum in C is known, so there are just $(2J+1)$ sub-states available in C. Thus, for the Breit-Wigner formula one can write more generally with a spin statistical factor

$$\sigma_{res,l}(1,2) = \omega\pi\bar{\lambda}^2 \frac{\Gamma_1 \Gamma_2}{(E - E_{res})^2 + \left(\frac{\Gamma}{2}\right)^2} \tag{2.30}$$

with

$$\omega = \frac{(2J+1)}{(2J_1+1)\cdot(2J_2+1)} \tag{2.31}$$

The reaction rates for a single narrow resonance can be calculated by the usage of equations (2.12) and (2.30) [4],

$$N_A \langle \sigma v \rangle = N_A \frac{\sqrt{2\pi}\hbar^2}{(\mu kT)^{3/2}}\, \omega \int_0^\infty \frac{\Gamma_1 \Gamma_2}{(E - E_{res})^2 + \left(\frac{\Gamma}{2}\right)^2}\, e^{-E/kT} dE \tag{2.32}$$

where N_A is the Avogadro constant.

For a sufficiently narrow resonance, the partial widths and the Maxwell-Boltzmann factor are almost constant over the total width of the resonance. They can be replaced by their value at E_{res} and the integral can be calculated analytically.
According to this [4]

$$N_A \langle \sigma v \rangle = N_A \left(\frac{2\pi}{\mu kT}\right)^{3/2} \hbar^2\, e^{-E_{res}/kT}\, \omega\gamma \tag{2.33}$$

where $\omega\gamma = \omega\, \Gamma_1\Gamma_2/\Gamma$ is used.

The resonant reaction rates are highly important in classical novae explosions, where resonant proton captures enhance nucleosynthesis. The actual good theoretical knowledge of the resonant proton capture rates on different nuclei results from the science of the properties of compound nucleus for resonant reactions: the partial widths of the excited state formed in the reaction, the energy of that state and the spin. The partial widths of an excited state can determined by measuring the life time of that state, because these two quantities are connected by equation (2.22)[2].

2.2 The Doppler Shift Attenuation Experiment

In the following section I will describe an experimental facility at the TU München for measuring the life times of excited nuclear states which aims to get better models of resonant reaction rates.

2.2.1 Motivation

Reactions in nova explosions involve proton capture into excited nuclear states of the compound nucleus thereby formed. As a example, one can think of the following reaction:

$$X + p \rightarrow Y^* \rightarrow Y + \gamma \tag{2.34}$$

where the asterisk expresses that nucleus Y is created in an excited nuclear state, which then almost instantly de-excites by gamma-ray emission, to the ground state of Y.

The purpose of the experiment that is set up by the experimental astrophysics group of the Institute E12 at the Technische Universität München is to determine the rates of these kinds of reactions, under physical conditions within nova explosions. Therefore it is essential to measure the life times of the excited nuclear states. This is done by using the Doppler shift attenuation method (DSAM).
The experimental facility is constructed at the Maier-Leibniz-Laboratory (MLL) located on the Garching campus of the Technische Universität München. At the laboratory there is a Van-de-Graaff tandem accelerator that achieves a maximum operating potential of 14 MV, and is able to accelerate stable beams ranging in mass from protons up to the actinide elements.

With a better knowledge of the life times of excited nuclear states, the theoretical models and predictions on the nucleosynthesis in nova explosions can be improved.

2.2.2 Experimental Method

The basic principle of the DSAM has been used successfully since the 1960's. It is used to determine life times ranging from 10^{-14} to 10^{-11} seconds[6].
In the experiment, the excited states of astrophysical interest in Y are created with a transfer reaction, schematically represented as:

$$Z + a \rightarrow Y^* + b \tag{2.35}$$

where Z is the accelerated ion and the nucleus a, can be a deuteron, ^3He, or an α particle. Y^* is excited into one of its astrophysically important states, and nucleus b called the transfer ejectile; again it is a particle, such as a proton, deuteron, ^3He, or an α particle (with a and b being different).
By measuring the ejectile particle b in coincidence with the gamma-rays from Y^*, the lifetime of the excited nuclear states can be determined, as will be explained shortly.

A target foil with high stopping power (e.g. gold) is implanted with the light target nuclei (particle a in the reaction above), such as ^3He or α particles. The gold foil has a thickness of about 15 microns and only the first 0.5 microns are implanted with the light nuclei ^3He at a density of about $4 \times 10^{17} \frac{\text{atoms}}{\text{cm}^2}$.

A beam of accelerated nuclei from the tandem accelerator at the MLL is directed onto the target foil and transfer reactions between the nuclei of the beam and the implanted nuclei happen. When this occurs, the nucleus Y in one of its excited states is produced somewhere in the first 0.5 microns of the target foil, along with the light ejectile particle b.

Making use of the two-body kinematics of the reaction, the populated excited state can be reconstructed by measuring the energy and the angle δ of the light ejectile. Figure 2.1 contains a sketch of the reaction process.

The excited nuclear state has a finite lifetime, though very short. The excited nucleus Y^* decays via gamma-ray emission while in motion and while slowing down in the target material. The gamma-rays will be Doppler shifted, because Y^* decayed while moving. Nevertheless, not every nucleus Y^* created in the experiment will decay with the same velocity, (or at the same time after being created) and therefore each has a different Doppler energy shift. The reason for this is that the probability that the excited state decays in a specific time interval has a decaying exponential time distribution. This is why not every Y^*nucleus decays at exactly the same time after being created.

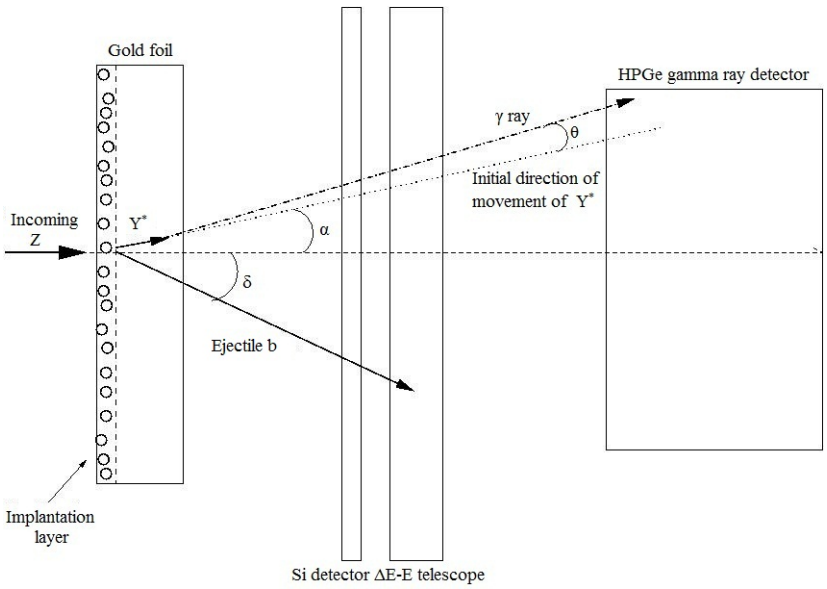

Figure 2.1: Schematic display of the DSAM reaction principle. Not to scale.

If the velocity $\beta = \frac{v}{c}$ of Y^* is significantly smaller than one, the following equation applies for the Doppler shifted γ-ray energy [7]:

$$E_\gamma = E_\gamma^0 \left[1 + F\left(\tau\right) \beta_\theta \left(0\right) \cos \Theta\right] \tag{2.36}$$

where E_γ is the γ ray energy (measured), E_γ^0 is the rest frame γ ray energy, $F\left(\tau\right)$ is the so-called attenuation coefficient that lies between 0 and 1, $\beta_\theta \left(0\right)$ is the initial velocity of Y^* at the time of creation and Θ is the γ-ray's angle of emission relative to the initial direction of Y^* at the moment of decay.
This equation now can be rearranged, to be,

$$\frac{E_\gamma - E_\gamma^0}{E_\gamma^0} = F\left(\tau\right) \beta_\theta \left(0\right) \cos \Theta \tag{2.37}$$

showing that the measured γ-ray distribution is related to the velocity distribution of the decaying nuclei. Knowing the stopping power of the target material for the considered nucleus, which gives us $\beta_\theta \left(t\right) \cos \theta$,almost the projected velocity distribution of this nucleus in the beam axis's direction.
Now, one can combine the decay exponential probability of Y^* and the velocity distribution to get the velocity distribution at the time of decay [7]:

$$F\left(\tau\right) \beta_\theta \left(0\right) = \frac{1}{\tau} \int_0^\infty \beta_\theta \left(t\right) \exp\left(-\frac{t}{\tau}\right) dt \tag{2.38}$$

This is the ideal representation for $F(\tau)$. However, this $F(\tau)$ must be convolved with the detector response function, which has a gaussian shape, as the measured E_{gamma} is not an exact energy value, but a energy distribution.

So as to be able to compare a Doppler shifted and a non-Doppler shifted gamma-ray spectrum, there are used three germanium detectors that are positioned in three different angles referring to the beam axis's direction.

Finally, the life time of the excited state can be obtained from this fit function with respect to τ [7].

2.2.3 Experimental Setup

The Doppler shift life time facility comprises a target chamber into which a copper target ladder constructed with 6 target holders is mounted. For beam diagnostics, a scintillation crystal is attached to the supreme target holder. It is used for tuning the beam onto the target. Furthermore, there is a movable mounting base for up to 3 silicon charged particle detectors placed in the target chamber.

Upstream of the target ladder is a copper tube of about 45 cm length that is concentrically oriented along the beam axis and extends to the target position. The tube is also in thermal contact with a liquid nitrogen (LN2) reservoir. The end of the tube that extends to the target has a copper block to which are affixed two copper leaf springs. These come into (thermal) contact with the target ladder, when the target ladder is raised into position.

Figure 2.2 shows a CAD rendering of the entire experimental setup.
The whole system can be pumped down to $\sim 10^{-7}$mbar. After the pressure in the system has dropped to this value with the aid of turbo pumps, the copper tube is cooled with LN2. This cooling of the tube effects adsorption of any remaining residual gas molecules onto its surfaces and improves the vacuum ("cold trap") inside the target chamber and the beam line. The target ladder at this time is elevated so that there is no thermal contact to the copper tube.

The target is cooled to avert diffusion of the implanted ^3He due to beam heating. Moreover, the target is raised into contact with the copper tube after sufficient time has passed to adsorb residual gas molecules upon the copper tube.

This is necessary to avoid contaminants on the surface of the targets that could otherwise react with the beam and be a potential source of unwanted background.

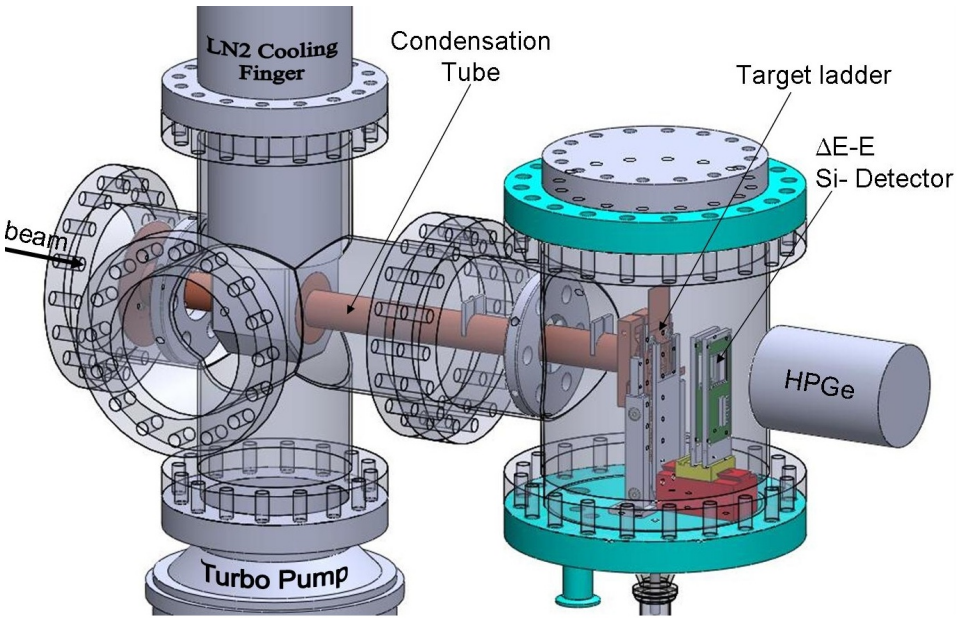

Figure 2.2: CAD rendering of the DSAM facility. Experiment design and visualization by Clemens Herlitzius.

Outside the target chamber the three germanium gamma-ray detectors are situated. Figure 2.3 shows a view from the top looking directly into the target chamber.

On the left side one can see the copper tube entering the target chamber and the copper block at the very end. Next, directly right of the copper block there is the target ladder.

On the right side of the target ladder, one sees the three mounting frames that hold the silicon detectors. With these monolithic detectors of different thickness, charged particles can be detected and their energy and position can be determined. The detectors form a position sensitive $\Delta E - E$ telescope with which the type of ejectile particle (proton, ^3He, α, etc.) can be identified and its energy and the scattering angle can be reconstructed.

As explained in this section, in the DSAM experiment the precise shape of the Doppler shifted γ ray spectrum provides the means to determine the life times of excited nuclear states. For that reason, good detection efficiency and a good knowledge of the detector response function is required.

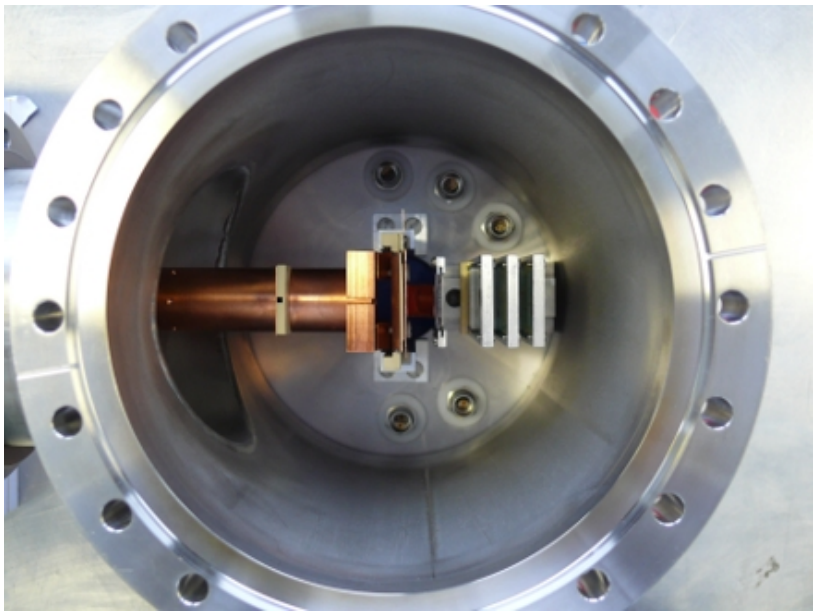

Figure 2.3: A view looking down into the target chamber, showing all essential parts.

2.3 High Purity Germanium Gamma-Ray Detectors

2.3.1 General Considerations

In semiconductor detectors, radiation is measured by collection of charge carriers set free in the detector, which is arranged between two electrodes. Radiation generates free electrons and holes. The energy transmitted to the detector is proportional to the number of electron-hole pairs in the semiconductor. A number of electrons are moved from the valence band to the conduction band, and conversely the same number of holes is created in the valence band. Under the influence of an electric field, the charge carriers travel to the (opposite) electrodes, where they trigger a pulse that can be measured in an outer circuit. The amount of energy that is necessary to create an electron-hole pair is proportional to the energy of the incoming radiation, so measuring the number of electron-hole pairs allows determining the energy of the incident radiation.

Compared with gaseous ionization detectors, the density of a semiconductor detector is very high, so charged particles of high energy can give off their total energy in a semiconductor of relatively small dimensions. In contrast to silicon detectors that cannot be thicker than a few millimeters, germanium can be used as a total absorption detector for gamma rays up to few MeV because of their greater depletion depth.

With increasing applied bias voltage, higher depletion depths can just be realized by reducing the net impurity concentration in the semiconductor material. With special refining techniques one can achieve an impurity concentration that is correlated to levels which are less than 1 part in 10^{12}. Detectors that achieve these levels are called *high purity germanium* (HPGe) detectors or intrinsic Detectors. They can have depletion depths up to several centimeters.

A handicap of Germanium detectors is that they have to be cooled to liquid nitrogen temperatures to produce spectroscopic data. At higher temperatures, the electrons can easily cross the Band gap in the crystal and reach the conduction band, where they are free to respond to the electric field. This reduces energy resolution. Cooling to liquid nitrogen temperature (77 K, but allowed to be somewhat higher) reduces thermal excitations of valence electrons so that only a gamma ray interaction can give an electron the required energy to reach the conduction band.

2.3.2 Coaxial Configuration

For planar detectors, the total germanium volume is limited. For producing detectors with larger volume as one prefers for gamma ray spectroscopy, detectors of a so-called coaxial geometry are chosen. One electrode is located at the outer surface of the cylindrical germanium crystal and the second electrode is constituted by removing the core of the cylinder and attaching a contact over the inner surface of the crystal. In combination with an elongated fabricated crystal this makes it possible to achieve large active volumes. Moreover, detectors with a coaxial configuration can be fabricated with lower capacitance than would be possible with planar geometry [1].

In the case of the so-called closed-ended coaxial configuration only the central core of the crystal is removed, so the outer electrode is extended over the one flat end of the crystal. This avoids the complications because of leakage currents at the front surface and provides a flat surface in the front that can be used as na entrance window for weakly penetrating radiation if a electrical contact is used.
In coaxial geometry it does not matter if the rectifying contact, which builds up the semiconductor junction, is placed at the outer or the inner surface of the detector. With the rectifying contact being placed at the outer surface, the depletion region moves inwards if the voltage is raised and it reaches the surface of the inner hole at depletion voltage. If the rectifying junction is on the inner surface, the depletion layer increases outwards but in this case one requires a much larger voltage to deplete the whole detector. Therefore the rectifying junction usually is placed at the outer surface.

Coaxial detectors with a central $n+$ contact are called n-type detectors, while p-type detectors have a $p+$ central contact. The thickness of these contacts represents a dead layer around the surface of the crystal within which energy depositions do not result in detector signals. A schematic comparsion of the n-type closed-ended and the more common p-type closed-ended HPGe is shown in figure 2.4

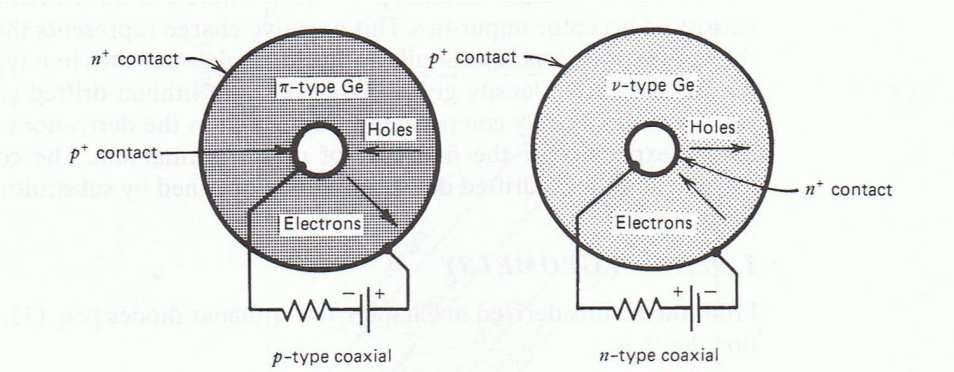

Figure 2.4: Schematic display of the positions of the electrodes and the directions into which holes and electrons are drifting in a coaxial HPGe detector of p- and n-type configuration. Source: [1]

The capacitance per unit length of a fully depleted true coaxial detector is given by

$$C = \frac{2\pi\epsilon}{\ln(r_2/r_1)} \tag{2.39}$$

whith the dielectric constant ϵ and with inner and outer radii r_1 and r_2[1]. Usually a minimal capacitance is preferred, so the inner radius r_1 is kept to a technical minimum.

2.3.3 Gamma Ray Spectroscopy

Good germanium detector systems have an energy resolution that is typically of a few tenths of a percent in comparison to 5-10% for sodium iodide scintillators. In consequence of this better resolution and the lower atomic number of the germanium detector, the photopeak efficiencies are perceptibly lower than typically. But the superior energy resolution that helps discriminate closely spaced peaks and the better detection of weak sources of discrete energies prevail this drawback.

That is why germanium detectors are definitely preferred for analyzing complex gamma ray spectra with a lot of peaks[1].

Evident in a gamma ray spectrum are typically X-rays from photoelectric absorptions, the backscatter peak, rudimentarily noticeable single escape (SE) and double escape (DE) peaks from pair production, the annihilation peak at 511 keV, the Compton edges and full-energy peaks from primary gamma rays, a sum peak due to the full absorption of both primary gamma rays and two small pile-up peaks.

Chapter 3

Characterization of the HPGe Detectors

In this chapter, I will present my best fit functions, energy calibration and efficiency measurements for the three HPGe detectors that are used in the experiment, for the γ-ray sources ^{22}Na, ^{60}Co and ^{207}Bi.

3.1 Description of the three HPGe Detectors

There are three HPGe detectors used in the experiment.

The first one is a closed-ended coaxial detector produced by Canberra.
It has an n-type configuration (negative electrode is on the lateral surface of the core hole), where the two electrodes are realized by dopant implementation. It is positioned at an angle of 60° relative to the beam axis' direction.

Figure 3.1 shows schematically the detector geometry. The germanium crystal has a specified length of 78.5 mm, the diameter is 79 mm, the core hole has a depth of 66 mm and a diameter of 13.5 mm.[8] The thickness of the outer electrode is 0.3 μm and the thickness of the inner electrode is 0.6 mm[8].

The crystal is placed inside of a 16 cm long aluminum cryostat of 1.5 mm thickness with an outer (measured) diameter of 9.52 cm. It is open to one side with a carbon epoxy window of 0.5 mm thickness and a measured diameter of 9 cm[8].

All quantities except of the ones that are specified as "measured" are taken from the Canberra data sheet of the detector[8].

The two other detectors are produced by ORTEC. The detectors have a specified length of 178 mm and the diameter is 90 mm.

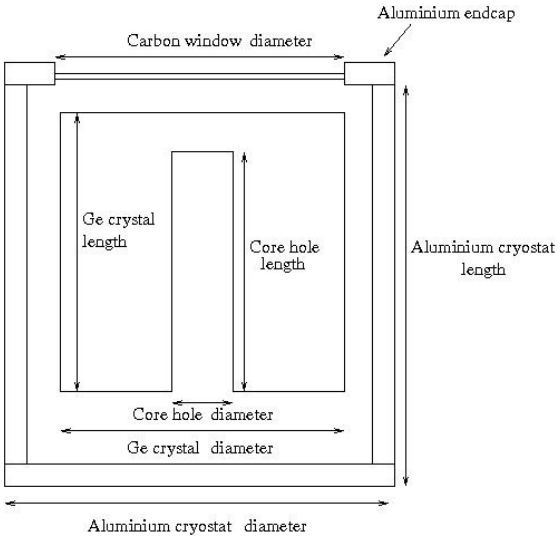

Figure 3.1: Schematic display of the germanium crystal of the detector, the core hole and the aluminium cryostat inclusive. Not to scale. Source: [2]

The one detector is positioned in an angle of 0° relative to the beam axis' direction (Model No.: GMX-90220-S ; Serial No.: 33-N40483A) an the second detector is positioned in an angle of 90° relative to the beam axis' direction (Model No.: GMX-90220-S ; Serial No.: 37-N31120A).

3.2 Method of fitting the Data

For the fitting method of the gamma ray spectra, the data analysis program and library ROOT developed by CERN was used. Macro scripts used by ROOT have been written for automating the process of characterization of HPGe gamma ray detectors.

Together with the gamma ray spectra, background spectra with a total runtime of 16 hours have been recorded and considered in the analysis. In the background spectra, there are peaks visible in the range of the photopeaks of the gamma ray spectra. However, these little peaks can be neglected in respect to the following equation, which is the ratio of their respective rates:

$$\frac{\Delta H_{bg}}{\Delta H_s} \cdot \frac{\Delta t_s}{\Delta t_{bg}} \tag{3.1}$$

where ΔH_{bg} and ΔH_s are the peak heights of the background peak and the photopeak and Δt_{bg} and Δt_s are the respective runtimes of the data recording.

As an example, the high energy peak of ^{60}Co, which is shown in figure 3.6, and the respective background spectrum, which is shown in figure 3.7, can be considered. In this case the ratio given by equation (3.1) has a value of 0.007%. That is why the analyzed spectra have not been background subtracted. The effect of the background peaks on the shape of the phtopeaks is negligible.

The physics and the statistics that determine the response of a germanium detector to a gamma ray source are complex, so a precise calculation of full-energy peak shapes is relatively difficult. A theoretical function is fitted to the full-energy peak experimental data points to represent the detector response near a full-energy peak. The function consists of a combination of five different functions. They represent a Gaussian that covers most of the full energy peak, a low energy exponential, a high energy exponential, a step function and a polynomial to express the background:

1. In the case of an ideal detector, a gamma ray with a negligible natural width would behave as a sharp, delta peak shaped response function. As a first term of the fit function, the totally absorbed component of a single peak has to be represented by a Gaussian, because that sharp delta line is broadened by the statistical nature of system noise and by the electric noise caused by the charge collection process:[9]-[10]

$$R_{Gaussian} = A \exp\left(-\left(\frac{x - x_0}{\delta}\right)^2\right) \tag{3.2}$$

where A is the amplitude, x_0 ist the position of the maximum of the photopeak and δ is the width of the peak.

2. Due to the incomplete charge collection and pile-up inside of the detector as well as electron escape, the Gaussian shape is distorted on its low energy tail, which means that in an ideal detector an exponentially decaying distribution on the low energy side of the peak is produced. That has to be folded with a Gaussian function accounting noise, thus providing a smooth cut-off. This results in a peak that has a roughly Gaussian shape but distorted or broadened on the low energy side of the peak[10]:

$$R_{lefttail} = B \exp\left(\frac{x - x_0}{\beta}\right) \operatorname{erfc}\left(\frac{x - x_0 + \frac{\gamma^2}{2\beta}}{\gamma}\right) \tag{3.3}$$

where B is the amplitude of this contribution to the peak, $erfc$ is the normalized complimentary error function, β defines the slope of the exponential distribution and γ is the slope of the complimentary error function, the so-called noise width.

3. Additionally, n-type HPGe detectors usually have also a "tail" on the high energy side of the peak (because of surface effects), which is similar to the one on the low energy side that is created by incomplete charge collection. The term representing this effect is again folded by a negative exponential function with a Gaussian shape[11]:

$$R_{righttail} = C \exp\left(\frac{x - x_0}{\kappa}\right) \text{erfc}\left(-\frac{x - x_0 + \frac{\tau^2}{2\kappa}}{\tau}\right) \tag{3.4}$$

where C is the amplitude, κ defines the slope of the exponential distribution and τ is the slope of $erfc$.

4. If the gamma rays have an energy more than about 2 MeV, pair-production plays an important role in the energy transfer to the detector. As a consequence, positron annihilation is resulting in two 511 keV gamma rays, where one or both of them can escape from the detector. Hence a source of single-energy gamma rays produces a full energy peak, a single-escape (peak 511 keV lower in energy) and a double-escape peak (1022 keV lower in energy). All of these have more or less different peak shapes.

Furthermore, the annihilation gamma ray is able to Compton scatter in the detector with an energy that is adding up to the escape peaks. Such summing effects generate a step or unsteadiness in the background below or above the peak. Likewise for low-energy gamma ray, a considerable step or ledge below the peak can be produced by Compton scattering from surrounding materials into the detector[12]:

$$R_{step} = D \text{ erfc}\left(\frac{x - x_0}{\sigma}\right) \tag{3.5}$$

where σ is the width and D is the amplitude that is usually set by subtracting the average hight of the background on the left side an the right side of the peak.
The choice of the step and the tailing have a significant effect on the goodness of the fit[9].

5. In a final step, the background term for the background continuum on both sides of the peak is presented by a polynomial of first or second order:

$$R_{polynomial} = a + b\,(x - x_0) + c\,(x - x_0)^2 \tag{3.6}$$

Terms 3 and 4, added with term 5, reveal a background with a sharp step at the peak and which decreases slowly below the peak.

Anyway, the variation of the background can be represented by a polynomial of suitable order and a step in the background about the peak channel, which is extending to the low energy side produced by the full-energy peak itself.

The analysis software ROOT can vary the height, the position and the width of the composite shape, as well as the background parameters. A peak area must be defined, so just the part of the spectrum within this range is going to be fitted[13].

The final function has a number of 15 parameters that must be varied to get the best fit function. The complete final fitting function is presented in appendix A.

It is a challenging task but it can be greatly simplified by choosing a good initial value for the parameters as a starting point for the optimization method. The fit of the peak is accomplished by the non-linear least squares method that searches the values of the fit parameters that minimize the sum of the squares of the deviations of the data (the residuals)from the fit function $F(x)$. The Chi-Square value

$$\chi^2 = \sum_i \frac{1}{\mathrm{ndf}} \left[y_i - F(x_i) \right] \tag{3.7}$$

is minimized, where x_i is the channel number, y_i the experimental data point and *ndf* is overall weighting factor given by the number of degrees of freedom in the fit, which is equal to the number of data channels included in the fit minus the number of free parameters. $F(x_i)$ values are determined from the fit function. The summation is accomplished over all the data point that are involved in the fit[9]-[11].

The characterization of the three HPGe detectors were accomplished by the usage of three different radioactive sources. Table 3.1 gives an overview of the used sources, the energies of those gamma ray lines that have an emission yield high enough for detection, their emission efficiencies and the associated source activities.

The complete spectra obtained for the three sources are presented in Figures 3.2, 3.3 and 3.4.

Source	Gamma Energy [keV]	Emission Probability	Source activity [kBq]
^{22}Na	1274.5	99.94%	61.80
^{207}Bi	569.7	97.75%	25.17
^{207}Bi	1063.7	74.50%	25.17
^{60}Co	1173	99.85%	154.30
^{60}Co	1332	99.98%	154.30

Table 3.1: Gamma sources used in the analysis, their gamma energies siutable for efficiency measurements, their emission probabilities and their activities.

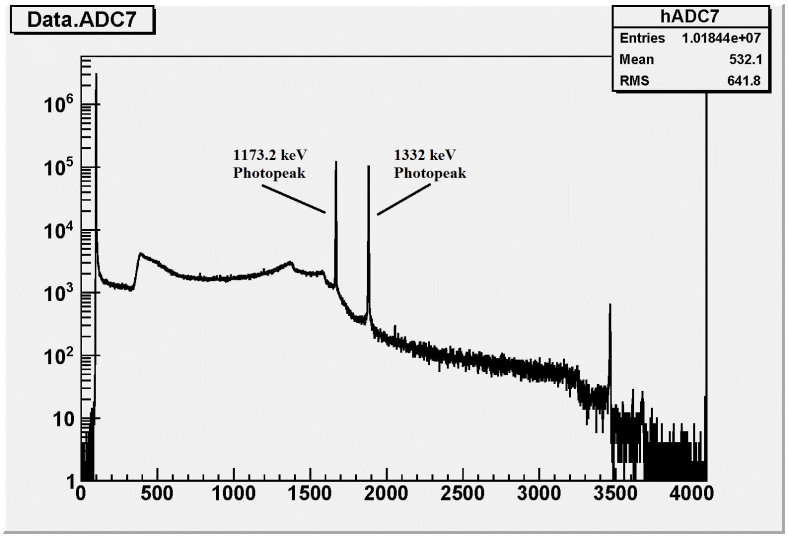

Figure 3.2: A spectrum of the gamma ray emission from the ^{60}Co source. This spectrum contains about 15 minutes of data.

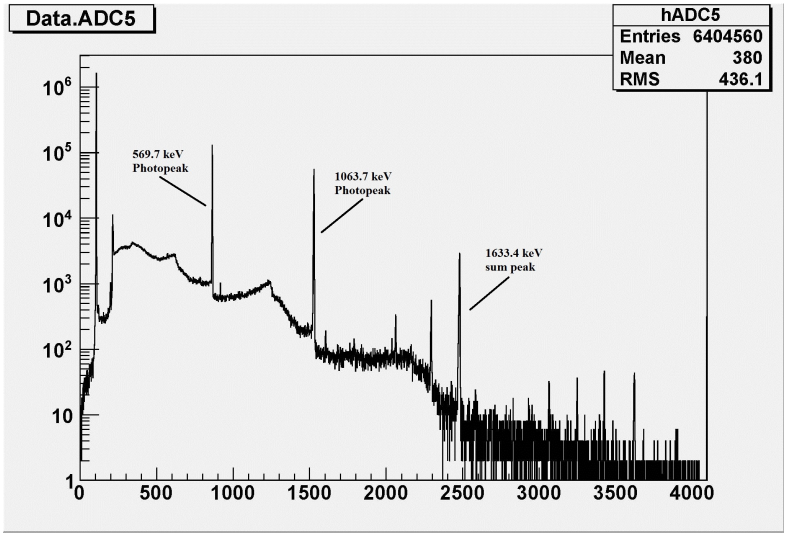

Figure 3.3: A spectrum of the gamma ray emission from the ^{207}Bi source. This spectrum contains about 40 minutes of data.

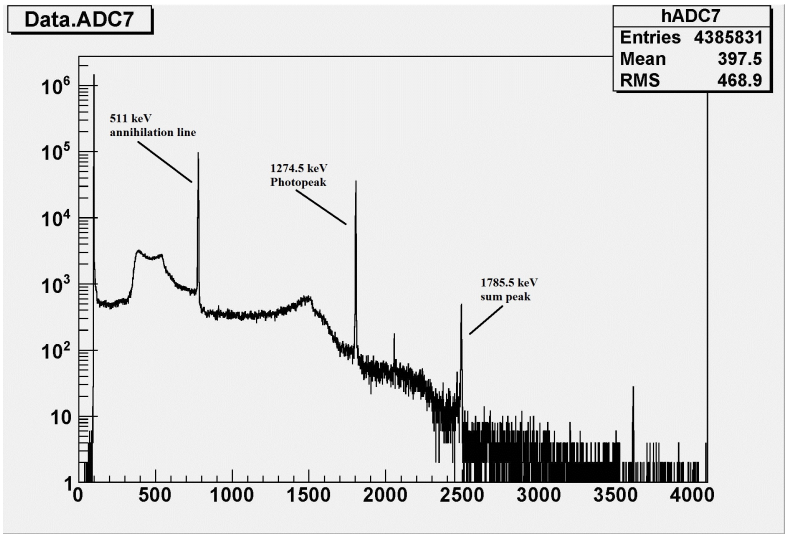

Figure 3.4: A spectrum of the gamma ray emission from the ^{22}Na source. This spectrum contains about 10 minutes of data.

Each of the peaks in Table 3.1 has been fitted with a individual combination of the described terms, but in most of the cases not all of the terms were necessary. In order to decide if the fit result is satisfying and physical, the used Root script for the fitting process has been designed in that way that the best fit function as well as a display of the full-energy peak in the spectrum, the fitting function and all the single components are given back. Thus, one is able to decide easily, whether the single terms of the fitting function behave physically.

Two examples of successful fits and their individual components can be seen in Figures 3.5 and 3.6. The precise values of the fit parameters of all fitted peaks are summarized in appendix A.

The figures that contain the graphical display of all other fitted Photopeaks are summarized in appendix B.

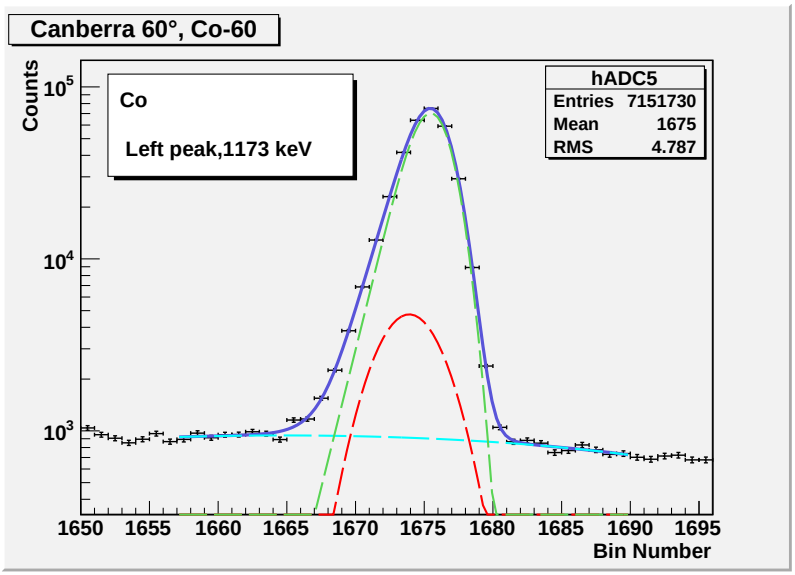

Figure 3.5: Example of a data fit using the fitting function described in this chapter. The 1173 keV photopeak of ^{60}Co along with the best fit function and its components for the Canberra detector. The goodness of the fit is χ^2 divided by the number of degrees of freedom $= 51.66/23 = 2.25$

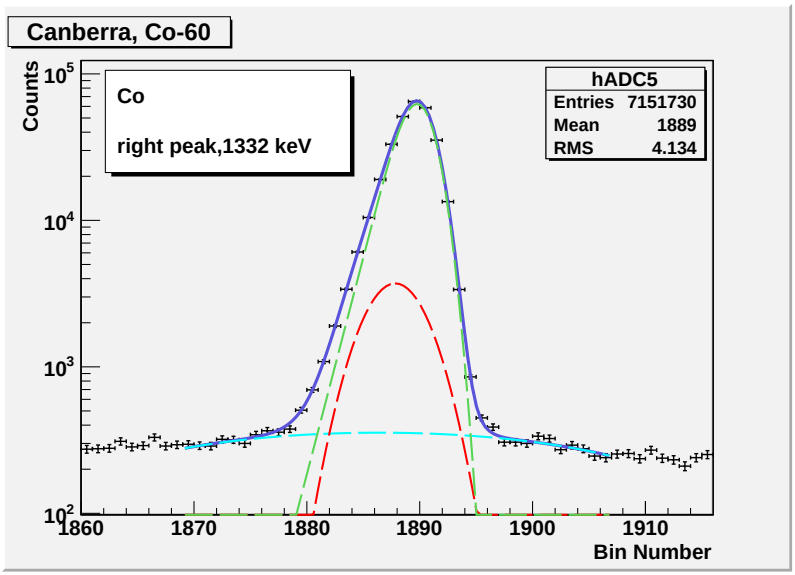

Figure 3.6: The 1332 keV photopeak of ^{60}Co along with the best fit function and its components for the Canberra detector. The goodness of the fit is χ^2 divided by the number of degrees of freedom = 41.2/28 = 1.47. This spectrum contains about 12 minutes of data.

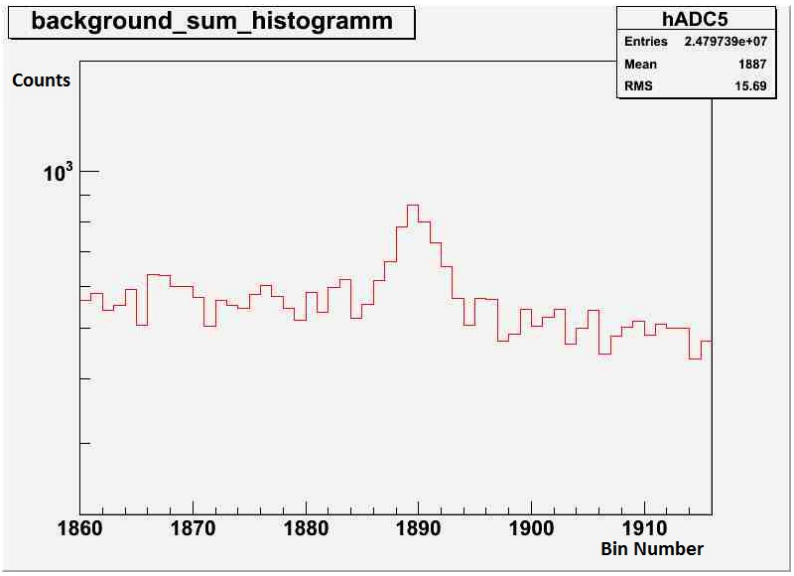

Figure 3.7: Background spectrum for the 1332 keV photopeak of ^{60}Co detected by the Canberra detector. This spectrum contains about 16 hours of data.

3.3 Results

In this section, I will present the results of the determination of the photopeak efficiency and the intrinsic efficiency as well as the determined energy calibration for the three detectors.

3.3.1 Efficiency

3.3.1.1 Definition

There are different possibilities for gamma rays entering the detector to deposit their energy: via photoelectric absorption, Compton scattering and pair production. It is dependent on the energy of the entering gamma as well as the material of the detector, which of those three processes is dominating within the detector. Usually a gamma ray of energy within the range of MeV does not deposit all of its energy in a single interaction. There can be more than one interaction between the detector material and one specific gamma and as well in many cases the gamma ray will escape from the detector without having deposited its entire energy.

Compton scattering is the most frequent form of interaction over a wide range of energy. In this case the gamma ray contributes to the *Compton continuum*, which is formed due to the circumstance that the incoming gamma can deposit any fraction of its energy while scattering. This behavior comes up because there are all scattering angles possible and the amount of energy loss by Compton scattering is dependent on the scattering angle.

The Compton continuum can be seen as component of the background which implies that the Compton continuum over higher energy peaks can overlap with the full-energy peak of a gamma rays with less energy, particularly if there are a lot of gamma rays from the same source.

According to the different possible ways of energy deposition by gamma rays in the detector, there different kinds of characterization of a detector's efficiency: The intrinsic efficiency states the probability to detect any gamma ray that is entering the detector:

$$\epsilon_{int} = \frac{\text{Number of detected gamma ray events}}{\text{Number of gamma rays entering the detector}} \tag{3.8}$$

For the total efficiency the solid angle that the detector covers referring to the source. This total efficiency states the probability to detect any gamma ray emitted by the source will interact within the detector:

$$\epsilon_{tot} = \frac{\text{Number of detected gamma ray events}}{\text{Number of gamma rays emitted by the source over } 4\pi \text{ steradians}} \tag{3.9}$$

The Photopeak efficiency states the probability that a gamma ray deposits its entire energy within the detector:

$$\epsilon_{photo} = \frac{\text{Number of detected gamma ray events in the photopeak}}{\text{Number of gamma rays emitted by the source over } 4\pi \text{ steradians}} \tag{3.10}$$

All these efficiencies are throughout calculated for a specific gamma energy that has to be stated with the efficiency value.

3.3.1.2 Findings

The Photopeak efficiency for each gamma ray line is determined by the usage of the software ROOT again.

First, the contents of all bins within the range of the peak, which has been set manually, are integrated. Then, the integral over the background components of the fit (polynomial term plus optionally the step) within the same range is subtracted. The obtained number of counts is then divided by the runtime of the measurement to get the rate in counts per second. Finally, the rate of the peak is divided by the activity of the source, which had been calculated before.

Every line has been corrected for its associated emission probability by multiplication of the nominal activity of the source with the emission probability before the number of counts in the Photopeak is divided by the activity.
The effect of the choice of the integration range on the number of counts in the peak has been checked by varying the integration range. The differences in the number of counts for the different ranges turned out to be negligible (around 0.1%).

The errors of the Photopeak efficiencies are determined by usage of the Gaussian error propagation of the statistical error of the number of counts in the Photopeak. It is given by the square root of this number and the error of the source activity that was estimated to be about 5% for all sources:

$$\sigma\left(\epsilon\right)^2 = \left(\left(\frac{\sqrt{N}}{N}\right)^2 \frac{1}{T} + \left(0.05\right)^2\right)^2 \tag{3.11}$$

with the total run time T, the Photopeak efficiency ϵ and the number of counts in the peak N[2].

In a next step the intrinsic efficiency is determined, which can be calculated by the usage of the following equation:

$$\epsilon_{int} = \epsilon_{photo} \cdot \frac{4\pi}{\Omega} \tag{3.12}$$

where Ω represents the solid angle (in steradians) subtended by the detector at the source position.

For the common case of a point source located along the axis of a circular cylindrical detector, Ω is given by

$$\Omega = 2\pi \left(1 - \frac{d}{\sqrt{d^2 + a^2}}\right) \tag{3.13}$$

where d is the source-detector distance and a is the radius of the detector surface that faces the source[1].

The source-detector distance of the three detectors is 8 cm, so the efficiency values are not normalized to the standard distance of 25 cm.

The errors of the intrinsic efficiency are calculated in the same way as it is done for the Photopeak efficiency.

The Photopeak efficiencies, the intrinsic efficiencies for all used gamma ray energies and their related errors for the three detectors are summarized in Tables 3.2, 3.3 and 3.4.

Source	Gamma energy [keV]	Photopeak efficiency and error	Intrinsic efficiency and error
^{22}Na	1274.5	(3.90 ± 0.20)E-03	(2.71 ± 0.14)E-02
^{207}Bi	569.7	(14.85 ± 0.74)E-03	(10.30 ± 0.51)E-02
^{207}Bi	1063.7	(10.28 ± 0.51)E-03	(7.13 ± 0.36)E-02
^{60}Co	1173	(2.95 ± 0.15)E-03	(2.04 ± 0.10)E-02
^{60}Co	1332	(2.74 ± 0.14)E-03	(1.90 ± 0.01)E-02

Table 3.2: Gamma ray sources, energies, photopeak efficiency with its associated errors and intrinsic efficiency with its associated errors for the Canberra detector.

Source	Gamma energy [keV]	Photopeak efficiency and error	Intrinsic efficiency and error
^{22}Na	1274.5	(3.84 ± 0.19)E-03	(2.29 ± 0.11)E-02
^{207}Bi	569.7	(13.59 ± 0.68)E-03	(8.10 ± 0.41)E-02
^{207}Bi	1063.7	(9.62 ± 0.48)E-03	(5.73 ± 0.29)E-02
^{60}Co	1173	(2.80 ± 0.14)E-03	(1.67 ± 0.08)E-02
^{60}Co	1332	(2.61 ± 0.13)E-03	(1.55 ± 0.08)E-02

Table 3.3: Gamma ray sources, energies, photopeak efficiency with its associated errors and intrinsic efficiency with its associated errors for the Ortec 0° detector.

Source	Gamma energy [keV]	Photopeak efficiency and error	Intrinsic efficiency and error
^{22}Na	1274.5	(3.21 ± 0.16)E-03	(1.91 ± 0.10)E-02
^{207}Bi	569.7	(11.00 ± 0.55)E-03	(6.56 ± 0.33)E-02
^{207}Bi	1063.7	(7.99 ± 0.40)E-03	(4.76 ± 0.24)E-02
^{60}Co	1173	(2.31 ± 0.12)E-03	(1.38 ± 0.07)E-02
^{60}Co	1332	(2.15 ± 0.11)E-03	(1.28 ± 0.06)E-02

Table 3.4: Gamma ray sources, energies, photopeak efficiency with its associated errors and intrinsic efficiency with its associated errors for the Ortec 90° detector.

3.3.2 Energy Calibration

As a last step, an energy calibration for the three HPGe detectors has been performed. All gamma rays that have been analyzed are used to find a best fit calibration function for the set up.

The energy calibration of the Canberra detector is determined by

$$E\,(bin) = 0.743\ \frac{\text{keV}}{\text{bin}} \cdot \text{bin} - 71.75\ \text{keV} \tag{3.14}$$

The energy calibration of the Ortec 0° detector is given by

$$E\,(bin) = 0.7434\ \frac{\text{keV}}{\text{bin}} \cdot \text{bin} - 67.74\ \text{keV} \tag{3.15}$$

Finally, the energy calibration of the Ortec 90° detector is expressed by

$$E\,(bin) = 0.7383\ \frac{\text{keV}}{\text{bin}} \cdot \text{bin} - 64.84\ \text{keV} \tag{3.16}$$

The plots of the three fit functions and the peak positions are shown in Figures 3.8, 3.9 and 3.10.

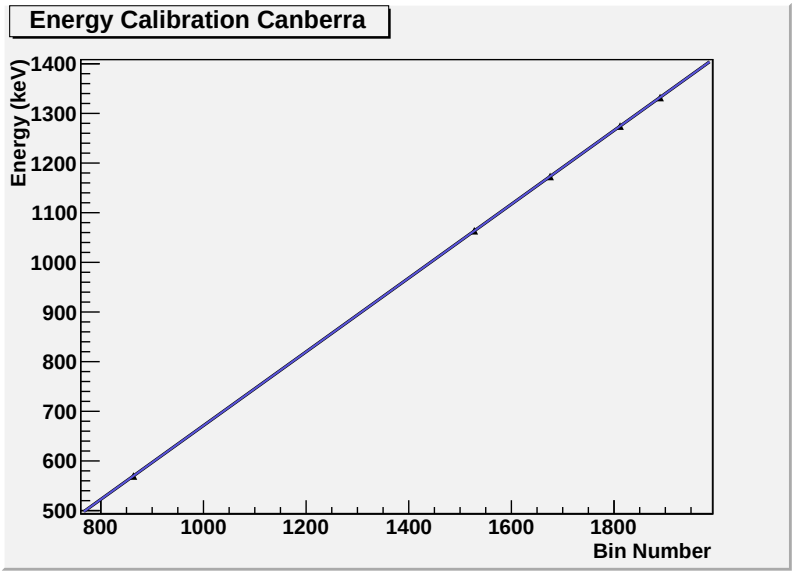

Figure 3.8: Best fit linear energy calibration function for the gamma ray peak positions, here for the Canberra detector

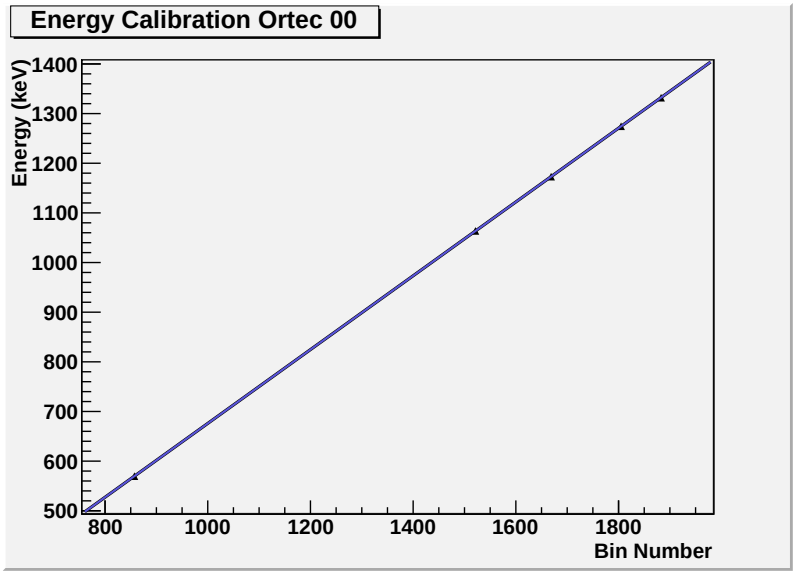

Figure 3.9: Best fit linear energy calibration function for the gamma ray peak positions, here for the Ortec 0° detector

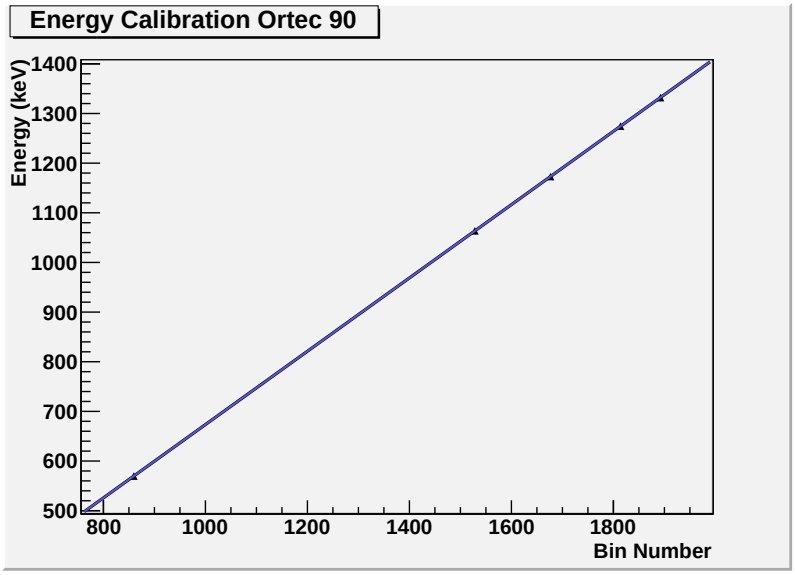

Figure 3.10: Best fit linear energy calibration function for the gamma ray peak positions, here for the Ortec 90° detector

Chapter 4

Conclusion

Within the frame of this Bachelor's thesis, I acquainted myself with the Doppler shift attenuation method and the experimental methods for characterizing HPGe detectors. I learned to work with the programming language C++ in an object-oriented way of programming at large and with the data analysis software ROOT in particular.

The experimental tasks of my thesis contained the determination of the Photopeak efficiency and the intrinsic efficiency as functions of energy, as well as the energy calibration for three HPGe detectors. Therefore, I have written macro scripts used by the software root for automating the process of characterization of HPGe gamma ray detectors. It tried to reduce the amount of analysis steps that have to be done manually. This process of automation can be further pressed ahead with in future for simplifying the characterization of HPGe gamma ray detectors.

The accurate knowledge of the detector properties as precise values of the fit parameters, the results of accurate efficiency measurements and an exact energy calibration will improve the accuracy of the DSAM experiment.

Especially, the results of my thesis are necessary to build up a precise Geant4 simulation of the whole DSAM experiment. Such a simulation allows it to simulate the in-flight decay of a decelerating ion within the thin target gold foil for the purpose of a simulation of DSAM gamma ray spectra. These spectra should be as real as possible. Therefore, my determined detector response functions are needed to generate a maximum realistic shape of the full-energy peaks that considers all the different effects on the peak's shape due to the detector's environment and the detector's inherent character, as well as statistical effects.

A complete and precise simulation of the whole experiment makes it possible that the consequences and results of future versions of the experiment or variations of the observed nuclear reaction can be estimated and predicted. Gamma ray spectra of future versions of the experiment can be verified and proved by comparing them to the simulations predictions.

Appendix A

Fit Functions

As discussed in chapter 3, the measured gamma ray spectra were received from the three sources used in the efficiency measurements. The full-energy peaks finally have been fitted using a function with different components. In the following, the parameters of the best fit functions for all five analyzed Photopeaks for all three detectors are presented, inclusive their respective errors. The parameters and their errors are calculated by the usage of ROOT scripts I have written. All the fit parameters have been numerated in the full fit function:

$$\begin{aligned} R_{fit} = \; & p_0 + p_1 \cdot (x - p_2) + p_3 \cdot (x - p_2)^2 + p_4 \exp\left(- \left(\frac{x - p_2}{p_5} \right)^2 \right) \\ & + p_6 \exp\left(p_7 \cdot (x - p_8) \right) \; \text{erfc} \; \left(\frac{x - p_8 + p_9^2 \cdot \frac{p_7}{2}}{p_9} \right) \\ & + p_{10} \exp\left(-p_{11} \cdot (x - p_{12}) \right) \; \text{erfc} \; \left(- \frac{x - p_{12} + p_{13}^2 \cdot \frac{p_{11}}{2}}{p_{13}} \right) \\ & + p_{14} \cdot \; \text{erfc} \; \left(\frac{x - p_2}{p_{15}} \right) \end{aligned} \tag{A.1}$$

The first line of the equation expresses the polynomial and the Gaussian, the second and third line express the high energy and low energy "tail" functions and the fourth line expresses the step function. For a more detailed explanation of the individual components, see section 3.2
In the tables, the entry "same as p_i" means that in the ROOT script this parameter and parameter p_i are one and the same for this fit. The entry "0 (fixed)" means that in the ROOT script this parameter has not been allowed to deviate from zero.

Fit parameter	Value with error for the best fit function
p_0	911.8 ± 24.9
p_1	-6.24 ± 0.59
p_2	1674 ± 0.3
p_3	-0.3389 ± 0.1343
p_4	4758 ± 627.7
p_5	3.358 ± 0.081
p_6	1.664e+05 ± 11271
p_7	0.7385 ± 0.0260
p_8	1676 ± 0.0
p_9	1.791 ± 0.016
p_{10}	0 (fixed)
p_{11}	0 (fixed)
p_{12}	0 (fixed)
p_{13}	0 (fixed)
p_{14}	0 (fixed)
p_{15}	0 (fixed)

Table A.1: Fit parameters, their respective best fit values and errors for the 1173 keV Photopeak of ^{60}Co for the Canberra detector

Fit parameter	Value with error for the best fit function
p_0	354.7 ± 11.9
p_1	-0.7241 ± 0.2700
p_2	1888 ± 0.2
p_3	-0.2596 ± 0.0499
p_4	3713 ± 435.5
p_5	3.803 ± 0.072
p_6	1.402e+05 ± 6727
p_7	0.6811 ± 0.0187
p_8	1891 ± 0.0
p_9	1.879 ± 0.013
p_{10}	0 (fixed)
p_{11}	0 (fixed)
p_{12}	0 (fixed)
p_{13}	0 (fixed)
p_{14}	0 (fixed)
p_{15}	0 (fixed)

Table A.2: Fit parameters, their respective best fit values and errors for the 1332 keV Photopeak of ^{60}Co for the Canberra detector

Fit parameter	Value with error for the best fit function
p_0	1505 ± 48.9
p_1	-20.73 ± 5.74
p_2	863.2 ± 0.1
p_3	0 (fixed)
p_4	3.958e+04 ± 27113
p_5	1.748 ± 0.055
p_6	1.177e+06 ± 310229
p_7	1.312 ± 0.062
p_8	864.1 ± 0.0
p_9	1.402 ± 0.027
p_{10}	0 (fixed)
p_{11}	0 (fixed)
p_{12}	0 (fixed)
p_{13}	0 (fixed)
p_{14}	106.8 ± 52.5
p_{15}	1.402 ± 0.027 (same as p9)

Table A.3: Fit parameters, their respective best fit values and errors for the 569.7 keV Photopeak of ^{207}Bi for the Canberra detector

Fit parameter	Value with error for the best fit function
p_0	300.4 ± 3.9
p_1	-5.859 ± 0.312
p_2	1528 ± 0.1
p_3	0 (fixed)
p_4	9.086e+04 ± 7776
p_5	1.746 ± 0.019
p_6	1.337e+05 ± 15506
p_7	0.8299 ± 0.0086
p_8	1527 ± 0.2
p_9	1.746 ± 0.019 (same as p5)
p_{10}	0 (fixed)
p_{11}	0 (fixed)
p_{12}	0 (fixed)
p_{13}	0 (fixed)
p_{14}	0 (fixed)
p_{15}	0 (fixed)

Table A.4: Fit parameters, their respective best fit values and errors for the 1063.7 keV Photopeak of ^{207}Bi for the Canberra detector

Fit parameter	Value with error for the best fit function
p_0	77.92 ± 2.65
p_1	0 (fixed)
p_2	1813 ± 0.0
p_3	0 (fixed)
p_4	0 (fixed)
p_5	0 (fixed)
p_6	8.598e+04 ± 5408
p_7	0.7502 ± 0.0273
p_8	1813 ± 0.0 (same as p2)
p_9	1.812 ± 0.013
p_{10}	7935 ± 2989.4
p_{11}	0.6329 ± 0.0488
p_{12}	1808 ± 0.3
p_{13}	3.703 ± 0.215
p_{14}	20.02 ± 1.90
p_{15}	1.812 ± 0.013 (same as p9)

Table A.5: Fit parameters, their respective best fit values and errors for the 1274.5 keV Photopeak of ^{22}Na for the Canberra detector

Fit parameter	Value with error for the best fit function
p_0	1178 ± 9.6
p_1	-5.317 ± 0.945
p_2	1669 ± 0.0
p_3	0 (fixed)
p_4	0 (fixed)
p_5	0 (fixed)
p_6	2.361e+05 ± 22475
p_7	0.9136 ± 0.0193
p_8	1669 ± 0.0 (same as p2)
p_9	1.564 ± 0.016
p_{10}	8.465e+05 ± 238932
p_{11}	1.531 ± 0.063
p_{12}	1668 ± 0.1
p_{13}	1.943 ± 0.034
p_{14}	0 (fixed)
p_{15}	0 (fixed)

Table A.6: Fit parameters, their respective best fit values and errors for the 1173 keV Photopeak of ^{60}Co for the Ortec 0° detector

Fit parameter	Value with error for the best fit function
p_0	415.5 ± 7.5
p_1	-1.693 ± 0.617
p_2	1883 ± 0.0
p_3	0 (fixed)
p_4	8.924e+04 ± 2890
p_5	1.852 ± 0.019
p_6	4.57e+04 ± 12240
p_7	0.8129 ± 0.0355
p_8	1882 ± 0.2
p_9	1.852 ± 0.019 (same as p5)
p_{10}	2.308e+04 ± 8774
p_{11}	0.6742 ± 0.0683
p_{12}	1881 ± 0.2
p_{13}	1.852 ± 0.019 (same as p5)
p_{14}	0 (fixed)
p_{15}	0 (fixed)

Table A.7: Fit parameters, their respective best fit values and errors for the 1332 keV Photopeak of ^{60}Co for the Ortec 0° detector

Fit parameter	Value with error for the best fit function
p_0	704.7 ±(fixed)
p_1	0 (fixed)
p_2	857.6 ± 0.0
p_3	0 (fixed)
p_4	0 (fixed)
p_5	0 (fixed)
p_6	1.718e+06 ± 98544
p_7	1.919 ± 0.022
p_8	857.6 ± 0.0 (same as p2)
p_9	1.267 ± 0.006
p_{10}	1.973e+04 ± 8226
p_{11}	1.4 ± 0.1
p_{12}	856.7 ± 0.1
p_{13}	0.883 ± 0.107
p_{14}	107.6 ± 5.8
p_{15}	1.267 ± 0.006 (same as p9)

Table A.8: Fit parameters, their respective best fit values and errors for the 569.7 keV Photopeak of ^{207}Bi for the Ortec 0° detector

Fit parameter	Value with error for the best fit function
p_0	114.9 ± 3.5
p_1	0 (fixed)
p_2	1521 ± 0.0
p_3	0 (fixed)
p_4	4.184e+04 ± 1357
p_5	1.625 ± 0.020
p_6	1.059e+05 ± 18101
p_7	1.051 ± 0.050
p_8	1522 ± 0.1
p_9	1.625 ± 0.020 (same as p5)
p_{10}	6999 ± 7326.1
p_{11}	0.7404 ± 0.1725
p_{12}	1520 ± 0.3
p_{13}	1.625 ± 0.020 (same as p5)
p_{14}	31.07 ± 2.7
p_{15}	1.625 ± 0.020 (same as p5)

Table A.9: Fit parameters, their respective best fit values and errors for the 1063.7 keV Photopeak of ^{207}Bi for the Ortec 0° detector

Fit parameter	Value with error for the best fit function
p_0	100.6 ± 3.1
p_1	-0.1859 ± 0.2646
p_2	1806 ± 0.0
p_3	0 (fixed)
p_4	0 (fixed)
p_5	0 (fixed)
p_6	7.928e+04 ± 6671
p_7	0.8809 ± 0.0208
p_8	1806 ± 0.0 (same as p2)
p_9	1.564 ± 0.022
p_{10}	2.234e+04 ± 4453
p_{11}	0.9646 ± 0.0499
p_{12}	1804 ± 0.1
p_{13}	1.564 ± 0.022 (same as p9)
p_{14}	0 (fixed)
p_{15}	0 (fixed)

Table A.10: Fit parameters, their respective best fit values and errors for the 1274.5 keV Photopeak of ^{22}Na for the Ortec 0° detector

Fit parameter	Value with error for the best fit function
p_0	821.4 ± 11.4
p_1	0 (fixed)
p_2	1677 ± 0.0
p_3	0 (fixed)
p_4	0 (fixed)
p_5	0 (fixed)
p_6	3.834e+05 ± 21928
p_7	1.028 ± 0.014
p_8	1677 ± 0.0 (same as p2)
p_9	1703 ± 0.009
p_{10}	4063 ± 4507.9
p_{11}	0.638 ± 0.200
p_{12}	1676 ± 0.5
p_{13}	1703 ± 0.009 (same as p9)
p_{14}	145.9 ± 8.4
p_{15}	1703 ± 0.009 (same as p9)

Table A.11: Fit parameters, their respective best fit values and errors for the 1173 keV Photopeak of ^{60}Co for the Ortec 90° detector

Fit parameter	Value with error for the best fit function
p_0	235.8 ± 13.7
p_1	-1.514 ± 1.134
p_2	1893 ± 0.1
p_3	0 (fixed)
p_4	3.514e+04 ± 9285
p_5	1.668 ± 0.046
p_6	1.185e+05 ± 20003
p_7	0.9874 ± 0.0145
p_8	1892 ± 0.1
p_9	1.668 ± 0.046 (same as p5)
p_{10}	2.194e+05 ± 65575
p_{11}	1.412 ± 0.113
p_{12}	1892 ± 0.2
p_{13}	1.668 ± 0.046 (same as p5)
p_{14}	50.08 ± 15.04
p_{15}	1.668 ± 0.046 (same as p5)

Table A.12: Fit parameters, their respective best fit values and errors for the 1332 keV Photopeak of ^{60}Co for the Ortec 90° detector

Fit parameter	Value with error for the best fit function
p_0	567.9 ± 16.9
p_1	-2.624 ± 2.923
p_2	863.3 ± 0.2
p_3	0 (fixed)
p_4	0 (fixed)
p_5	0 (fixed)
p_6	2.332e+06 ± 168711
p_7	1.993 ± 0.026
p_8	860 ± 0.0
p_9	1.388 ± 0.004
p_{10}	0 (fixed)
p_{11}	0 (fixed)
p_{12}	0 (fixed)
p_{13}	0 (fixed)
p_{14}	171 ± 26.2
p_{15}	1.388 ± 0.004 (same as p9)

Table A.13: Fit parameters, their respective best fit values and errors for the 569.7 keV Photopeak of ^{207}Bi for the Ortec 90° detector

Fit parameter	Value with error for the best fit function
p_0	133.4 ± 2.9
p_1	-3.874 ± 0.290
p_2	1528 ± 0.0
p_3	0 (fixed)
p_4	5.16e+04 ± 2046
p_5	1.719 ± 0.014
p_6	5.988e+04 ± 8250
p_7	1.199 ± 0.047
p_8	1528 ± 0.2
p_9	1.719 ± 0.014 (same as p5)
p_{10}	0 (fixed)
p_{11}	0 (fixed)
p_{12}	0 (fixed)
p_{13}	0 (fixed)
p_{14}	0 (fixed)
p_{15}	0 (fixed)

Table A.14: Fit parameters, their respective best fit values and errors for the 1063.7 keV Photopeak of ^{207}Bi for the Ortec 90° detector

Fit parameter	Value with error for the best fit function
p_0	45.45 ± 8.98
p_1	-0.2299 ± 0.6557
p_2	1815 ± 0.0
p_3	0 (fixed)
p_4	0 (fixed)
p_5	0 (fixed)
p_6	8.218e+04 ± 13833
p_7	0.9713 ± 0.0379
p_8	1815 ± 0.0 (same as p2)
p_9	1.677 ± 0.015
p_{10}	4485 ± 9573.9
p_{11}	0.9245 ± 0.4254
p_{12}	1813 ± 0.4
p_{13}	1.677 ± 0.015 (same as p9)
p_{14}	15.49 ± 10.06
p_{15}	1.677 ± 0.015 (same as p9)

Table A.15: Fit parameters, their respective best fit values and errors for the 1274.5 keV Photopeak of ^{22}Na for the Ortec 90° detector

Appendix B

Graphic Displays of the Fits

In the following, the graphical display of the Photopeaks used for the efficiency measurements, along with the best fit function and their single components, are summarized. The successful fits for the 1173 keV and the 1332 keV Photopeak of ^{60}Co for the Canberra detector have already been shown in section 3.2
For the best fit function and its single components, the following colour coding has been used: the dark blue solid line represents the best fit function, cyan has been used for the background, red for the Gaussian, green for the low energy tail, pink for the high energy tail and yellow has been used for the step function.

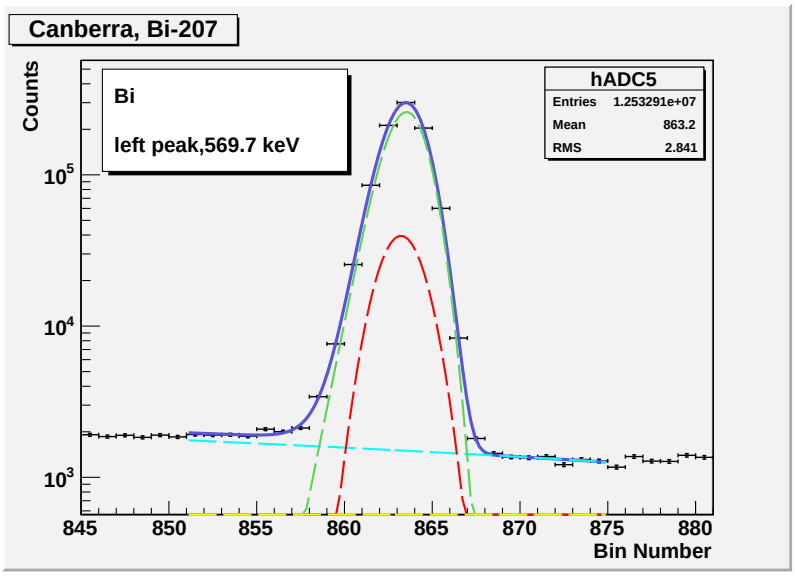

Figure B.1: The 569.7 keV photopeak of ^{207}Bi along with the best fit function and its components for the Canberra detector. The goodness of the fit is χ^2 divided by the number of degrees of freedom $= 41.07/14 = 2.93$

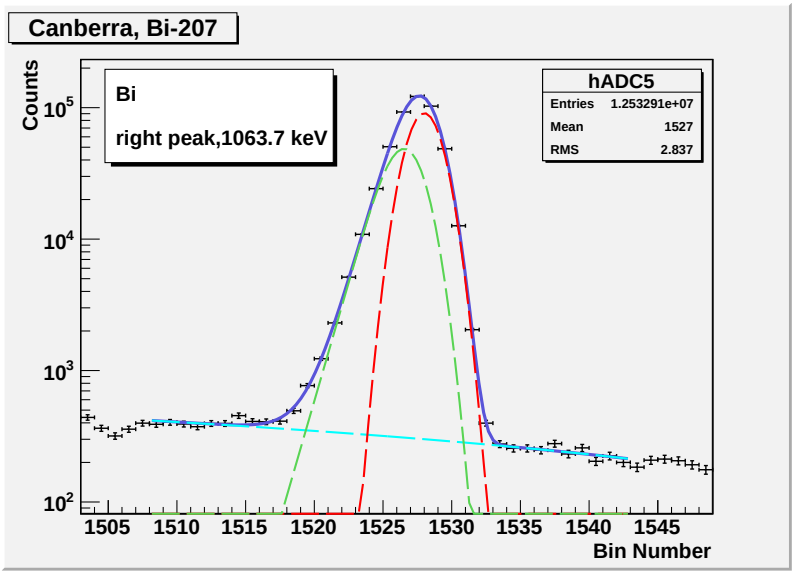

Figure B.2: The 1063.7 keV photopeak of ^{207}Bi along with the best fit function and its components for the Canberra detector. The goodness of the fit is χ^2 divided by the number of degrees of freedom $= 52.48/27 = 1.94$

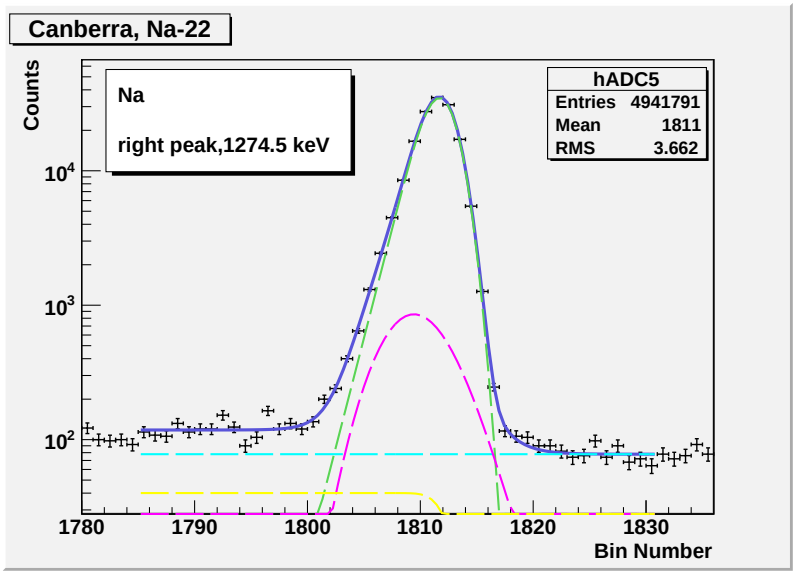

Figure B.3: The 1274.5 keV photopeak of ^{22}Na along with the best fit function and its components for the Canberra detector. The goodness of the fit is χ^2 divided by the number of degrees of freedom $= 83.12/36 = 2.31$

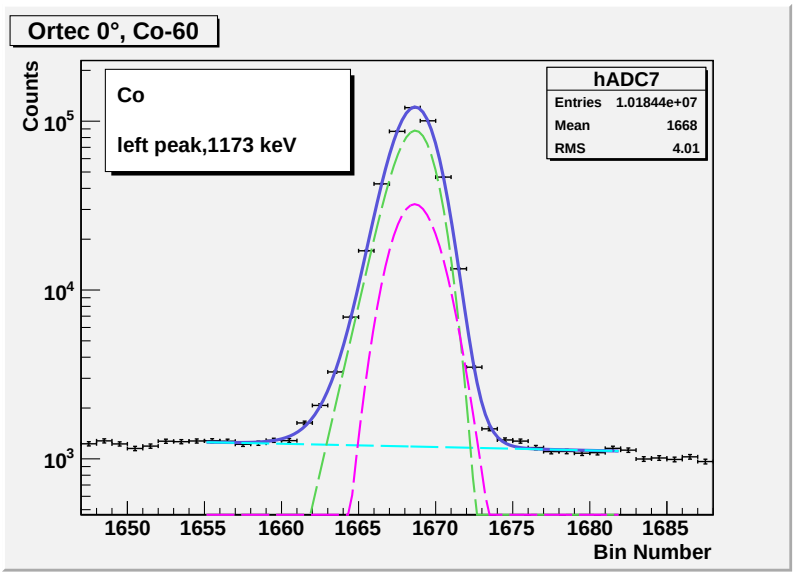

Figure B.4: The 1173 keV photopeak of ^{60}Co along with the best fit function and its components for the Ortec 0° detector. The goodness of the fit is χ^2 divided by the number of degrees of freedom = 37.95/17 = 2.23

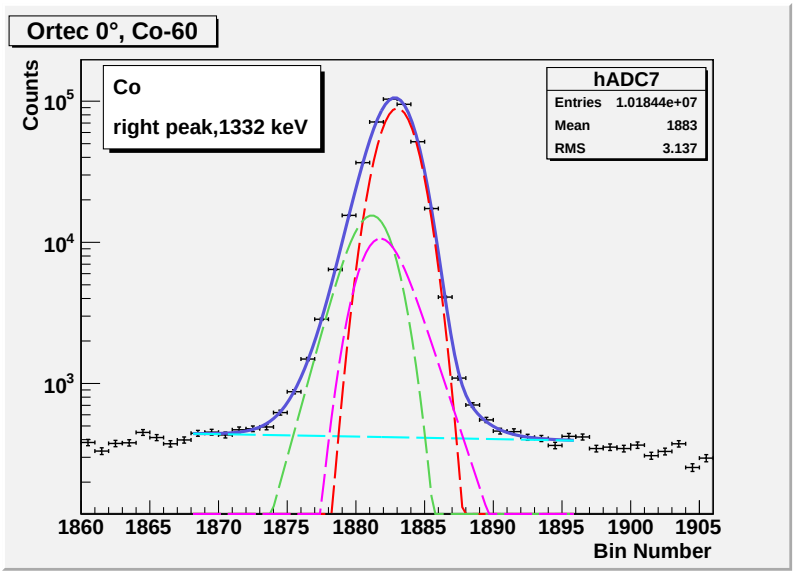

Figure B.5: The 1332 keV photopeak of ^{60}Co along with the best fit function and its components for the Ortec 0° detector. The goodness of the fit is χ^2 divided by the number of degrees of freedom = 35.03/17 = 2.06

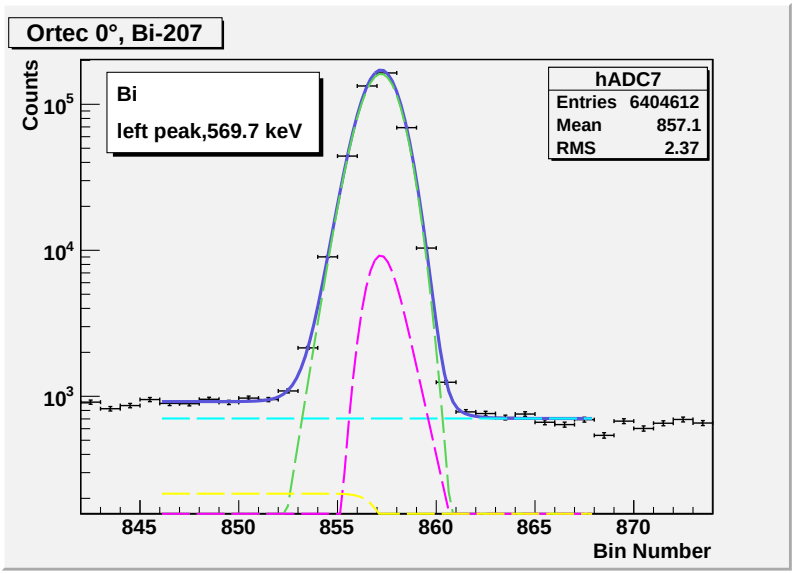

Figure B.6: The 569.7 keV photopeak of ^{207}Bi along with the best fit function and its components for the Ortec 0° detector. The goodness of the fit is χ^2 divided by the number of degrees of freedom = 22.46/13 = 1.73

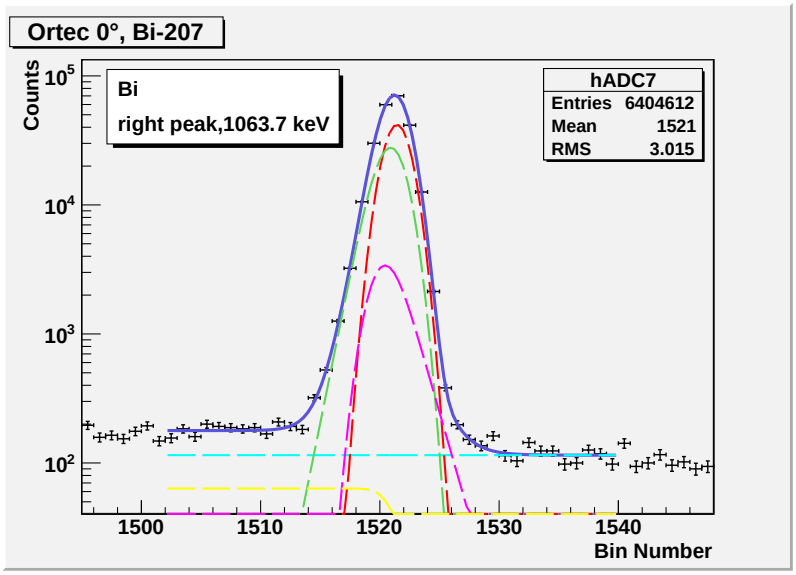

Figure B.7: The 1063.7 keV photopeak of ^{207}Bi along with the best fit function and its components for the Ortec 0° detector. The goodness of the fit is χ^2 divided by the number of degrees of freedom = 67.01/27 = 2.48

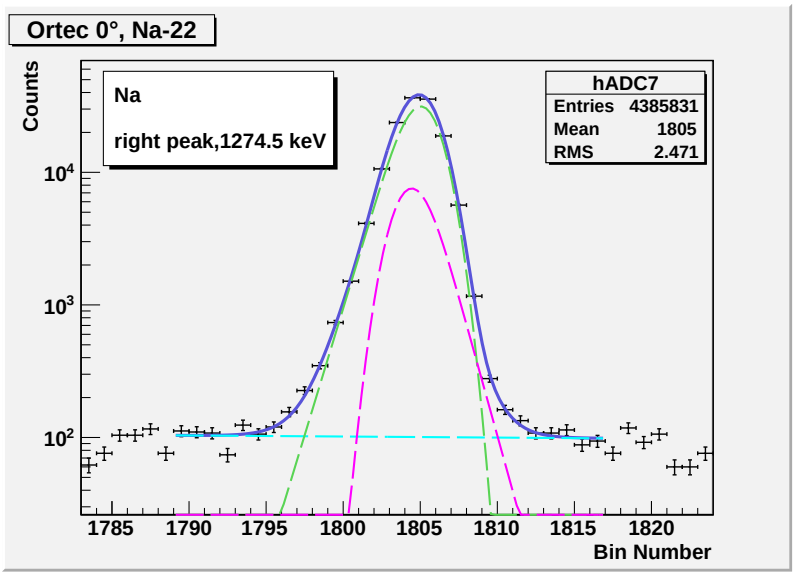

Figure B.8: The 1274.5 keV photopeak of ^{22}Na along with the best fit function and its components for the Ortec 0° detector. The goodness of the fit is χ^2 divided by the number of degrees of freedom = 46.53/19 = 2.45

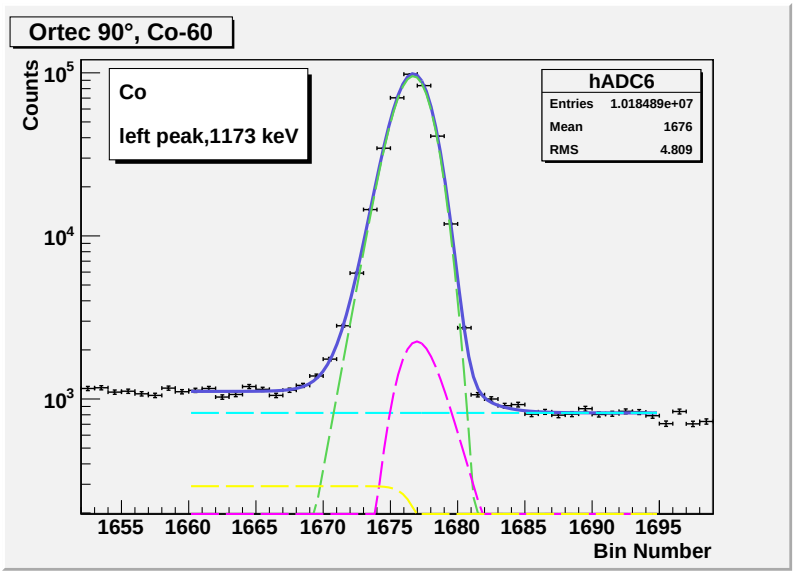

Figure B.9: The 1173 keV photopeak of ^{60}Co along with the best fit function and its components for the Ortec 90° detector. The goodness of the fit is χ^2 divided by the number of degrees of freedom = 59.35/26 = 2.28

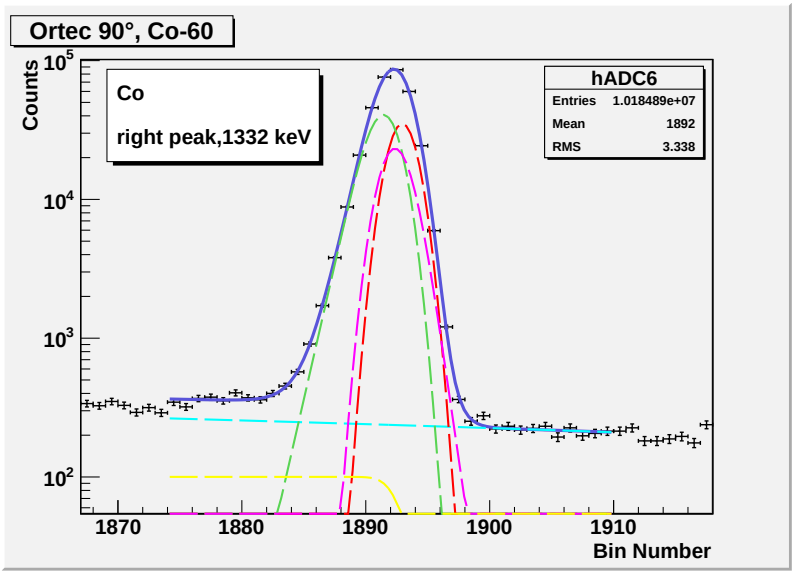

Figure B.10: The 1332 keV photopeak of ^{60}Co along with the best fit function and its components for the Ortec 90° detector. The goodness of the fit is χ^2 divided by the number of degrees of freedom $= 32.44/24 = 1.35$

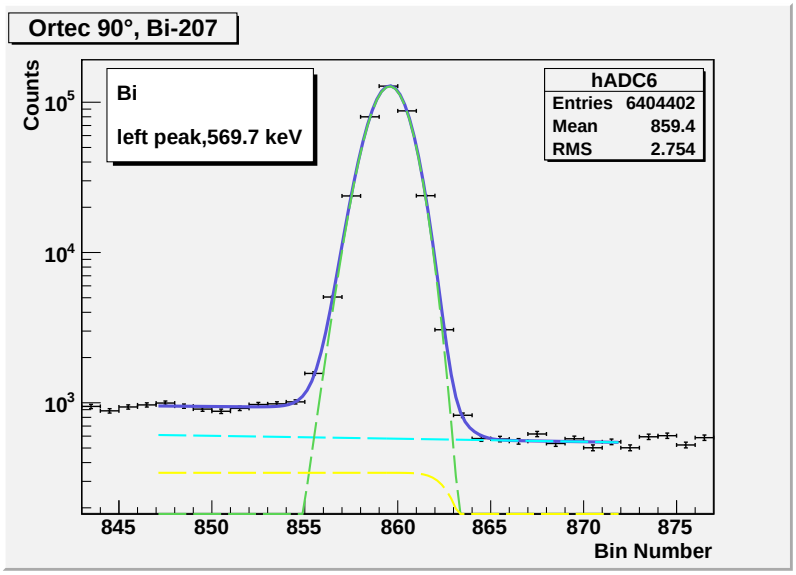

Figure B.11: The 569.7 keV photopeak of ^{207}Bi along with the best fit function and its components for the Ortec 90° detector. The goodness of the fit is χ^2 divided by the number of degrees of freedom $= 37.72/17 = 2.22$

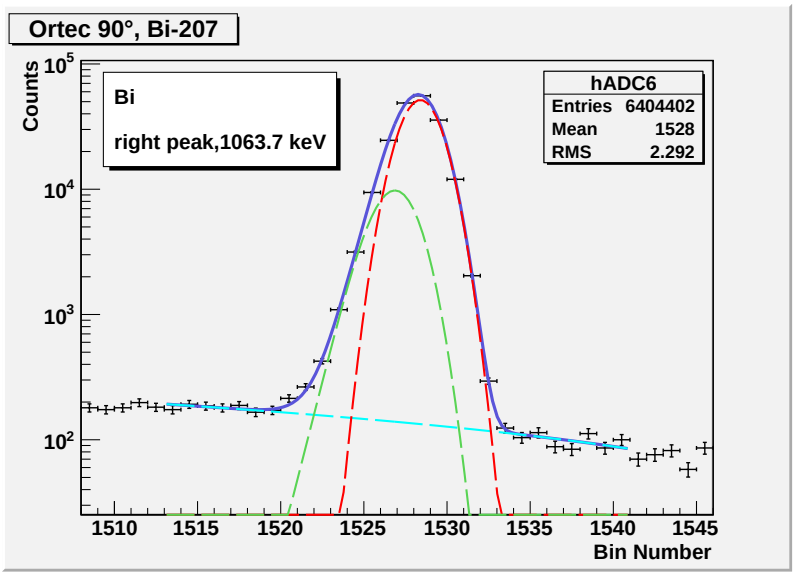

Figure B.12: The 1063.7 keV photopeak of ^{207}Bi along with the best fit function and its components for the Ortec 90° detector. The goodness of the fit is χ^2 divided by the number of degrees of freedom $= 38.02/20 = 1.90$

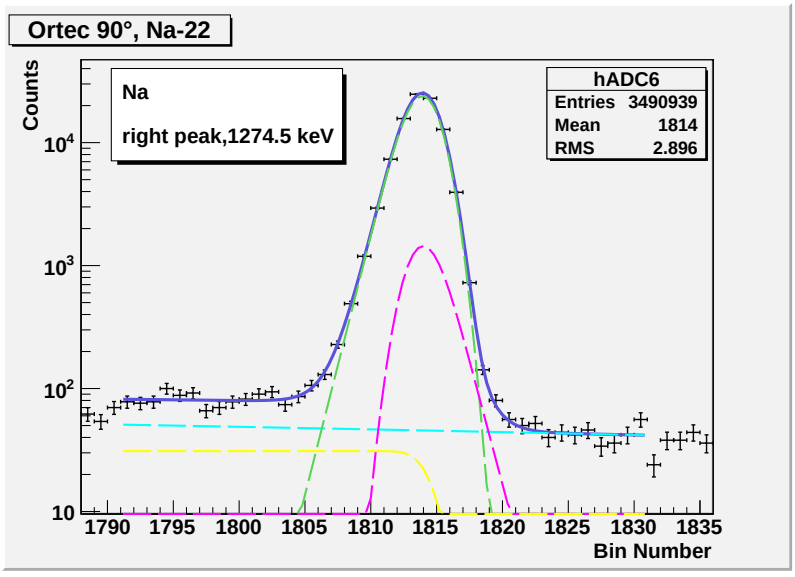

Figure B.13: The 1274.5 keV photopeak of ^{22}Na along with the best fit function and its components for the Ortec 90° detector. The goodness of the fit is χ^2 divided by the number of degrees of freedom $= 40.01/30 = 1.33$

Bibliography

[1] Knoll, Glenn F.: *Radiation Detection and Measurement.* Wiley, 4. edition, (2010).

[2] Fiehl, Janina: *Calibration of a HPGe Detector and Geant4 Simulation for a Doppler Shift Attenuation Experiment.* Diplomarbeit, Technische Universität München, (2010).

[3] Murdin, Paul: *Encyclopedia of Astronomy and Astrophysics.* Institute of Physics Publishing/Nature Publishing Group, 1. edition, (2001).

[4] Iliadis, Christian: *Nuclear Physics of Stars.* WILEY-VCH, 1. edition, (2007).

[5] Clayton, Donald D.: *Principles of Stellar Evolution and Nucleosynthesis.* The University of Chicago Press, 2. edition, (1983).

[6] Blaugrund, A.E.: *Notes on Doppler-Shift Lifetime Measurements.* Nuclear Physics 88, 501-512, 1966.

[7] E.J. Hoffman, D.M. van Patter, D.G. Sarantites J.H. Barker: *Line Shapes of Doppler Sfiffted γ-Rays from Coincidence and Singles Spectra in Measurements of Nuclear Lifetimes.* Nuclear Instruments and Methods 109, 3-11, 1973.

[8] *Design diagram S/N 10540 "Inner Drawing n-type".*

[9] S. I. Najafi, T. Kikindai: *Analytical Approximation of the Gamma Ray Spectra from Germanium Detectors.* Journal of Radioanalytical Chemistry 68, No. 1-2, 127-134, 1982.

[10] Ciftcioglu Özer: *An Analytical Approximation to the Peaks Obtain from Ge(Li) and Si(Li Detectors Used in Gamma Spectrum Analysis).* Nuclear Instruments and Methods 174, 209-220, 1980.

[11] L. C. Longoria, J. S. Benitez: *Full Energy Peak Efficiency of a Ge Detector as a Fucntion of Energy and Distance.* Appl. Radiat. Isot. 47, No. 3, 339-343, 1996.

[12] Gary W. Phillips, Keith W. Marlow: *Automatic Analysis of Gamma-Ray Spectra from Germanium Detectors.* Nuclear Instruments and Methods 137, 525-536, 1976.

[13] Robinson, D. C.: *A Computer Programme for the Determination od Acuurate Gamma Ray Line Intensities from Germanium Spectra.* Nuclear Instruments and Methods 78, 120-124, 1970.

Acknowledgement

In the end I want to thank all those who have supported me during my activity at the MLL and the Institute E12 as well as in writing this thesis. Special thanks go to:

Prof. Dr. Shawn Bishop, for providing me the opportunity to accomplish my Bachelor's thesis in the astrophysical group at the Institute E12 and for all his support and advice. He invested plenty of time in me and my work, so I profited a lot by his great knowledge and experience. I really felt welcome in his group.

Clemens Herlitzius, who explained me with great patience all the details of my tasks and teached me how to work with the programm ROOT. He was always available for me and with his competent method of working and his knowledge he helped me a lot. Especially at the beginning of my work, he invested much time in answering all my questions and helping me with all my problems.

Martin Wagner, for helping me with all the little pitfalls and problems with LaTeX during authoring this thesis.

All the members of the experimental astrophysics group and the rest of the E12 college and the MLL college not mentioned before, that have seen to it that I have had a very comfortable working environment.

My family and my friends who have always encouraged me and exceptionally my parents who have made my studies possible and have supported me in all respects.